Case Studies in Thermal Engineering 61 (2024) 104940

Contents lists available at ScienceDirect

Case Studies in Thermal Engineering

journal homepage: www.elsevier.com/locate/csite

Bayesian neural networks for solar power forecasts in advanced thermoelectric systems

Hisham Alghamdi [a], Chika Maduabuchi [b,*], Kingsley Okoli [b], Abdullah Albaker [c], Mohammad Alobaid [d,**], Mohammed Alghassab [e,***], Emad Makki [f,g], Mohammad Alkhedher [h]

[a] Electrical Engineering Department, College of Engineering, Najran University, Najran, 55461, Saudi Arabia
[b] Artificial Intelligence Laboratory, University of Nigeria Nsukka, Nsukka 410001, Enugu, Nigeria
[c] Department of Electrical Engineering, College of Engineering, University of Ha'il, Ha'il, 81451, Saudi Arabia
[d] Department of Mechanical and Industrial Engineering, College of Engineering, Majmaah University, Al-Majmaah, 11952, Saudi Arabia
[e] Electrical Engineering Department, College of Engineering, Shaqra University, Riyadh, 11911, Saudi Arabia
[f] Department of Mechanical Engineering, College of Engineering and Islamic Architecture, Umm Al-Qura University, Makkah, 24382, Saudi Arabia
[g] Department of Ocean and Resources Engineering, School of Ocean and Earth Science and Technology, University of Hawaii at Manoa, Honolulu, HI, 96822, USA
[h] Department of Mechanical and Industrial Engineering, Abu Dhabi University, Abu Dhabi, 59911, United Arab Emirates

ARTICLE INFO

Keywords:
Segmented thermoelectric modules
Solar energy Harvesting
Skutterudite optimization
Neural Network modeling
Thermal parametric analysis

ABSTRACT

This study presents a Bayesian neural network for the comprehensive performance forecast of an advanced thermoelectric system featuring segmented thermocouples with variable area shape for optimal solar energy conversion. The training data is obtained from a three-dimensional numerical model developed in ANSYS software to account for the energy, exergy, and entropy flows in the thermoelectric module to maximize the power output, energy, and exergy efficiencies while minimizing the entropy generation and system irreversibilities. The thermodynamic model optimizes key parameters, including geometry (height, cross-section, and percentage skutterudite content) across realistic diverse heat fluxes and cooling coefficients. To facilitate a faster and more efficient optimization pipeline, various neural networks, leveraging algorithms like Levenberg-Marquardt, scaled conjugate gradient, and Bayesian regularization, are utilized for efficient data management and accurate performance prediction. The Bayesian neural network emerges as the most accurate and efficient model providing the lowest training and testing loss of $\sim 10^{-9}$. Furthermore, key findings highlight the importance of skutterudite content and solar concentration ratio. For instance, an optimal skutterudite content of 6.2 % at 25 Suns produces maximum power of 29.7 W, while 37 % skutterudite at 75 Suns minimizes exergy destruction. This study's methodology and findings contribute to designing more efficient clean energy systems and advancing sustainable energy goals.

* Corresponding author.
** Corresponding author.
*** Corresponding author.
E-mail addresses: chika.maduabuchi.191341@unn.edu.ng (C. Maduabuchi), m.alobaid@mu.edu.sa (M. Alobaid), malghassab@su.edu.sa (M. Alghassab).

https://doi.org/10.1016/j.csite.2024.104940
Received 19 April 2024; Received in revised form 2 August 2024; Accepted 4 August 2024
Available online 5 August 2024

Nomenclature

Abbreviation

ANN	Artificial neural network
iTe	Bismuth telluride
BR	Bayesian regularization
COD	Coefficients of determination
FEM	Finite element method
LM	Levenberg-marquardt
MLP	Multilayer perceptron
MSE	Mean square error
PbTe	Lead telluride
R^2	Coefficient of determination
RSS	Residual sum of squares
SCG	Scaled conjugate gradient
SKT	Skutterudite
STEGs	Segmented thermoelectric generators
SVAL TEGs	Segmented variable area leg thermoelectric generators
TEGs	Thermoelectric generators
TSS	Total sum of squares

Symbols

A_{mod}	Surface area (mm^2)
C_{opt}	Optical solar concentration ratio
G	Solar irradiance (W/m^2)
$h_{conv,c}$	Cold junction convective film coefficient (kW/m^2K)
$h_{conv,h}$	Hot junction convective film coefficient (W/m^2K)
I	Identity matrix
$\overrightarrow{J}$	Local current density
k	Thermal conductivity (W/mK)
η_a	Absorption efficiency
η_{en}	Energy efficiency
η_{ex}	Exergy efficiency
η_{opt}	Optical efficiency
η_{te}	Thermoelectric efficiency
ρ	Electrical resistivity (Ω·m)
P	Search direction vector
P_{te}	Power output (W)
Q_c	Heat out (W)
Q_{in}	Heat flux on the ceramic plate at the hot end (W)
Q_h	Heat in (W)
q_{out}	Cooling effect of the cold junction (W)
R^2	Coefficient of determination value
S	Seebeck coefficient (V/K)
T	Absolute temperature (K)
T_{film}	Film Temperature (K)
T_s	Sun temperature (K)
τ	Thomson coefficient (V/K)
T_a	Air temperature (K)
T_c	Cold junction temperature (K)
w	Wind speed (m/s)
w_i	Weight associated with input i
W	Vector of weights and biases
v_k	Weighted sum of the inputs
x_i	Input signal
y_i	Target output
y_i'	Predicted output for the i^{th} data point
ZT	Figure of merit (−)
α	Step size

β	Conjugate gradient update parameter
$\phi(v_k)$	Output of the sigmoid activation function
λ	Damping factor
δ	Parameter update vector

Subscripts

conv,c	Cold junction convective film coefficient
conv,h	Hot junction convective film coefficient
c	Cold junction temperature
d	Destruction
gen	Generation
in	Input
opt	Optical
re	Regularized
te	Thermoelectric

1. introduction

The increasing energy scarcity and growing emphasis on environmental conservation have sparked global initiatives to research and develop sustainable, eco-friendly energy alternatives. One such solution is thermoelectric technology, which utilizes semiconductors to directly convert heat into electricity, attracting significant attention. In addition to its manageable noise pollution, this technology boasts numerous benefits, such as compact size, lightweight construction, affordable operation, outstanding reliability, and environmental compatibility.

The performance of thermoelectric materials is assessed using the figure-of-merit, $ZT = S^2 T/\rho k$, where S stands for the Seebeck coefficient, ρ indicates electrical resistivity, k symbolizes thermal conductivity, and T represents the absolute temperature at which thermoelectric properties are determined. Higher ZT values can substantially improve the power output and conversion efficiency of thermoelectric generators (TEGs). As materials with a ZT value greater than 1 are typically deemed commercially viable, enhancing ZT continues to be a primary objective for thermoelectric researchers and manufacturers. Various strategies have been proposed to increase ZT, such as element doping, developing multi-scale microstructures, and modifying atomic and molecular structures in thermoelectric semiconductors [1]. Li et al. [2] synthesized a series of Yb-single skutterudites with an increased filling fraction limit of 0.5, compared to 0.3 in standard $CoSb_3$, leading to a lower k of 1.75 $Wm^{-1}K^{-1}$ at 600 K and a high ZT of 1.34 at 780 K. Yanagisawa et al. [3] decreased the k of the Si membrane in a poly-Si TEG by 60 % using a 300 nm nano-patterning technique based on the mean free path spectrum of thermal phonons. This alteration doubled the ZT of the unpatterned membrane, while increasing its temperature gradient, resulting in four times and ten times higher voltage and power density, respectively.

In the past two decades, the field of thermoelectric materials has seen significant advancements, with some documented ZT values nearing 4 [4]. It is important to understand that ZT is not constant; instead, it is primarily expressed as a temperature-dependent polynomial function that varies depending on the thermoelectric material and does not consistently increase with rising operating temperatures. As a result, there is an optimal temperature range for achieving high ZT values for each thermoelectric material. This classification leads to thermoelectric materials being categorized into high-temperature materials, medium-temperature materials, and low-temperature materials [5]. Tetradymites, initially studied in the 1950s [6] and typically composed of $(Bi,Sb)_2(Te,Se)_3$, are a common family of TE compounds used for near room temperature applications. They have the R $\overline{3}$ m crystal structure and perform optimally within the 300–500 K temperature range [7]. Notably, Bi_2Te_3 (BiTe) alloys exhibit high ZT values of 1.2 at 357 K [8] and 1.4 at 373 K [9] for n- and p-type semiconductors, respectively. The material's ZT declines when the TEG operates at temperatures beyond the optimal range. Medium temperature materials (500–900 K) primarily consist of lead salts used for power generation applications. More recently, skutterudites (SKT) and tetrahedrites have also been classified as middle temperature materials, with n-SKT reaching peak ZT values of 1.7 at 850 K [10] and p-PbTe (lead telluride) 2.2 [11] at 915 K. For high temperature materials (>900 K), lower ZT values greater than 1 have been reported for SiGe and FeNSb-based alloys [12]; however, similar conversion efficiencies to medium temperature materials can be achieved due to the higher temperature gradient.

When concentrating solar TEGs operate at high solar concentrations and, consequently, high temperatures, using a single TE material in the semiconductor's legs may not efficiently cover the entire operating temperature range. This limitation also applies to TEGs used in automotive waste heat recovery systems, where operating temperatures can surpass 1000 K under maximum load conditions [13]. To address this issue, the first functionally graded/segmented TEG (STEG) was developed, and several efforts were made to maximize its efficiency by optimizing the height of the semiconductors [14]. Kuznetsov et al. [15] achieved a 10 % efficiency across an applied temperature gradient of 223 K–423 K using a segmented Bi_2Te_3 TEG, which outperformed the standard Bi_2Te_3 TEG. The STEG was created by joining two melted Bi_2Te_3 materials with peak ZT values at 270 K and 380 K, using the Bridgman method and a double doping technique. The p-type thermocouple was fabricated from a solid solution of $((Bi_2Te_3)_{0.25}(Sb_2Te_3)_{0.72}(Sb_2Se_3)_{0.03}$, doped with 2–4 wt% Te and 0.05–0.2 wt% SbI_3, while the n-type material consisted of a solid solution $(Bi_2Te_3)_{0.7}(Sb_2Te_3)_{0.25}(Sb_2Se_3)_{0.05}$.

Current research on STEGs can be classified into three main areas, as summarized in Supplementary file Table S1. The review demonstrates that the performance improvements offered by STEGs compared to traditional TEGs using uniform materials have been well-established.

The design of the TE pins' structure plays a crucial role in determining the overall performance of a TEG. Existing research has explored the impact of various geometric factors, such as TE height and cross-sectional area, on the device's performance. Fan et al. [16] introduced a 1D mathematical model for determining the optimal leg length and area ratios under fixed thermal boundary conditions. Luo and Kim [17] utilized a numerical model in ANSYS to examine the influence of cross-sectional area ratios and contact resistance on a two-stage TEG's performance, finding that a maximum efficiency of 8.7 % was achieved when the area ratio between the cold and hot stages was 1.1 (almost unity). Yusuf et al. [18] created a 1D mathematical model for TEG geometry optimization using a genetic algorithm, considering electrical and thermal contact resistances. They reported a maximum power and efficiency of 30.1 W and 9.87 % at 500 K, respectively. Ferreira-Teixeira and Pereira [19] employed a 3D FEM model in COMSOL to investigate the optimal geometry parameters for a TEG, discovering that under a fixed thermal gradient of 47 K, an optimal height-width ratio of 0.005 existed.

Commercially available TEGs typically feature rectangular-shaped pins with uniform cross-sectional areas along the vertical axis of the leg length. However, alternative leg geometries with varying cross-sectional areas have been proposed to enhance TEG performance. One of the earliest efforts to introduce variable area leg TE couples (VAL TECs) for improved power and efficiency was made by Soviet researcher Ioffe in his book [20]. Brandt [21] utilized Ioffe's equations to provide computer solutions to the governing equations of VAL TECs. Subsequently, Ali et al. [22] performed an exergy analysis of VAL TECs featuring an X-leg geometry configuration. Ibeagwu [23] employed a 3D numerical model in COMSOL to demonstrate that, given fixed hot and cold junction temperatures of 420 K and 300 K, respectively, the X-leg TEG generated 19.13 % more power than its rectangular leg counterpart. Fabián-Mijangos et al. [24] conducted the first experimental fabrication of a VAL TEG with nine couples, reporting a twofold increase in ZT compared to a conventional TEG.

Recently, a few studies have aimed to combine segmentation and variable area leg geometry to enhance TEG performance [25] and further studies deployed double-stage segmentation for similar goal. The motivation behind these studies was the assumption that since STEGs and VAL TEGs demonstrated superior performance compared to traditional TEGs, an appropriate combination of both technologies could result in a high-performing TEG. The first attempt at segmented variable area leg TE couples (SVAL TECs) was made by Liu et al. [26] using a 3D numerical model developed in COMSOL Multiphysics for solar energy applications. The authors presented a generalized model to predict the optimal leg length ratio for any leg shape TEG. They noted that, for an optimal leg length ratio of 2.5:3.5, the maximum power of the STEG (0.0855 W) improved by 4.21 % when using VAL TECs. All simulation results were conducted for a fixed concentrated solar flux of 65.1 kWm^{-2}. These innovative findings motivated Shittu et al. [27] to use the same software and numerical model to optimize the SVAL TEC's geometry for minimum von-Mises stress in the legs while maintaining high power under rectangular pulsed heating conditions. The researchers found that the power output was maximized at an optimum height ratio of 0.2. Subsequently, Zhang et al. [28], reported that the optimal performance of a TEG for a specified volume can only be achieved by combining segmented variable area legs to form an SVAL TEG. They also demonstrated that, for a temperature gradient of 300 K, the output power of the SVAL TEG was 51.71 % and 7.57 % higher than that of conventional and variable area leg TEGs, respectively.

Optimizing TEGs for concentrated solar power necessitates a meticulous exploration of pivotal parameters, particularly those governing heat fluxes and cooling coefficients. These factors, such as the solar concentration ratio and convective heat transfer coefficients, wield substantial influence over TEG performance metrics - power output, efficiency, and reliability. The intricate interplay between these parameters demands a depth of understanding beyond the reach of conventional methods. Traditional experimental approaches often grapple with capturing the non-linear dynamics inherent in TEG systems, while analytical methods may struggle with accurately modeling complex geometries and thermal interactions. Recognizing these challenges, our research introduces an innovative methodology that seamlessly integrates numerical analysis and Artificial Neural Networks (ANNs) to provide a comprehensive understanding of key parameters with enhanced accuracy, efficiency, and versatility. In essence, the solar concentration ratio plays a pivotal role in determining the intensity of solar irradiance incident on TEG modules, directly impacting power output. Simultaneously, convective heat transfer coefficients are critical for characterizing heat dissipation, profoundly influencing system efficiency and reliability. The constraints of traditional methodologies emphasize the necessity for our innovative strategy, integrating in-depth numerical simulations to investigate thermal and geometric complexities, coupled with the predictive capabilities of ANNs to capture intricate relationships.

Some recent applications of neural networks in accurately and efficiently forecasting the performance of thermoelectric systems are highlighted. Zhu et al. (2022a) utilized ANNs to simulate the functionality of a TEG based on finite element-derived data. Additionally, Bamisile et al. [29] employed deep learning algorithm to construct a model for the accurate prediction of solar irradiance and solar photovoltaic system. Beyond precision, this synergistic methodology significantly reduces time and resource requirements, accelerating the optimization processes vital for advancing renewable energy technology. In the current literature, there's a recognized potential in improving the performance of thermoelectric generators by employing segmented and non-uniform cross-section pins. However, there are notable limitations in the existing research that open up room for significant advancements.

1. **Simultaneous Utilization of Segmented and Non-uniform TE Elements**: While the exceptional performance of segmented materials and non-uniform TE elements is widely recognized, only a handful of studies with restrictive scopes and overly simplified assumptions have attempted to concurrently harness the benefits of these two methods to augment the efficacy of TE generators. This points towards a significant opportunity for more comprehensive and practical research in this domain, paving the way for the development and implementation of these innovative devices.

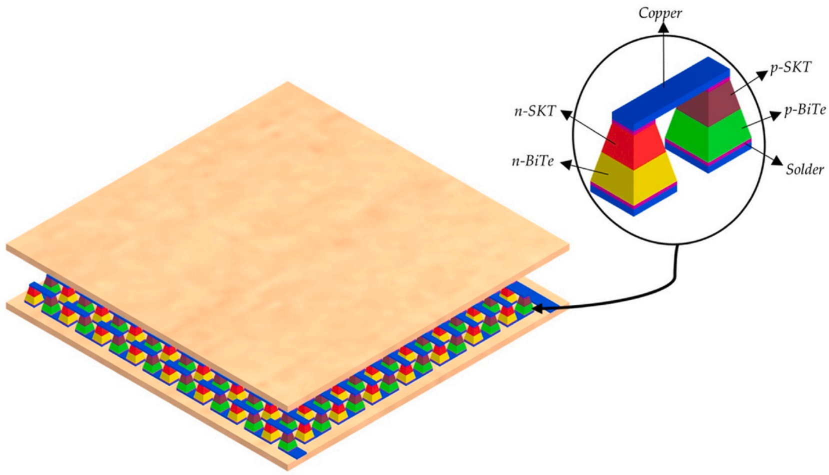

Fig. 1. Conceptual model of the Thermoelectric System Featuring Segmented Thermoelectric Couples with Variable Area.

2. **Comprehensive Second Law Assessments**: Comprehensive exergy analysis and entropy minimization, crucial for a complete second law assessment, are overlooked in studies that explore the combination of segmented and non-uniform cross-section TE elements.
3. **Analysis of Full-scale TE Modules**: Several studies analyze single TE elements in isolation, thereby ignoring the mutual thermal and electrical interaction among the multitude of TE elements in a realistic module. This omission leads to inaccurate performance estimations that are inapplicable in real life situations.
4. **Realistic Boundary Conditions**: Most existing studies present their optimization insights based on isothermal boundary conditions, which don't accurately reflect the conditions of a solar energy conversion system typically subjected to dynamic concentrated solar heat fluxes and convective heat transfer coefficients.

Addressing these identified gaps, our study offers a comprehensive and realistic approach.

1. **Comprehensive 3D Analysis of Full-scale TE Module**: This study presents a comprehensive three-dimensional finite element analysis enacted in ANSYS software on a full-scale TE module. The module comprises 254 TE elements, each segmented (using bismuth telluride for low-temperature material and skutterudite for high-temperature material) with a non-uniform cross-sectional area (trapezoidal shape) along the length. This approach encapsulates the advantages of segmented and non-uniform area TE elements, giving a realistic performance estimation.
2. **Realistic and Dynamic Boundary Conditions**: We substitute the commonly adopted constant temperature conditions with dynamic concentrated solar heat fluxes at the hot junction and convective heat transfer coefficients at the cold junction, creating a more realistic representation of a solar energy conversion system.
3. **Optimization of Geometry and Solar Energy Parameters**: Our study delves deeper into the optimization of thermoelements' geometry parameters and solar energy-related parameters. We optimize semiconductor height, cross-sectional area, skutterudite content, hot junction convective heat transfer coefficient, and ambient temperature from energy, exergy, and entropy perspectives across diverse heat fluxes and convective cooling coefficients.
4. **Efficient Forecasting via Neural Networks**: To expedite the time-intensive computational process, we propose several neural networks. These networks, relying on advanced algorithms like Levenberg-Marquardt, scaled conjugate gradient, and Bayesian-regularization, serve as efficient, timely, and accurate means of forecasting the performance of the proposed system.

In essence, our study aims to provide a comprehensive thermodynamic analysis of a novel TE system for solar energy conversion applications, delivering an innovative blueprint for its sustainable design while supporting global sustainable energy objectives. The in-depth analyses and unique perspectives presented in this study aim to expedite the manufacturing and design process, thus representing a significant advancement in the field.

2. Methodology

This section encompasses the description of the concentrating SVAL TEM and delves into the theoretical foundations of the finite element method for the SVAL TEM. Moreover, it elaborates on the equations employed to determine the energy, exergy, and entropy performance parameters of the device. Subsequently, further section covers the principles behind the artificial neural network models, elucidates the performance metrics, and offers a concise overview of the computational resources utilized for the numerical analysis.

2.1. Model conceptualization

In the proposed SVAL TEM system, the module is designed with 127 thermocouples electrically connected in series and thermally in parallel as depicted in Fig. 1. Each thermocouple consists of two semiconductor legs, one n-type and one p-type, with different materials for the upper and lower sections. The upper semiconductors are made of n- and p-type skutterudite, while the lower semiconductors are composed of n- and p-type bismuth telluride. The system is housed between two ceramic plates, with the upper plate exposed to concentrated solar flux. As the solar flux is absorbed, it creates a temperature gradient between the upper and lower ceramic plates, driving the thermoelectric power generation through the semiconductor legs. The geometry of the semiconductor legs is optimized by considering the height, cross-sectional area, and percentage content of SKT and BiTe materials. The optimization process accounts for the combined impacts of solar flux and geometry parameters on the performance of the device, ensuring the most efficient power generation possible. To accurately model the temperature gradients and power generation in the system, a comprehensive analysis is performed, including energy, exergy, and entropy considerations. This analysis considers various thermal parameters, such as the solar concentration ratio, convective cooling film coefficients, hot junction convective heat transfer coefficient, and ambient temperature, to determine the optimal performance of the module under different operating conditions.

2.2. *Thermoelectric finite element method coupled equations in ANSYS software*

The FEM is a powerful numerical technique employed for solving partial differential equations in complex domains. In the context of thermoelectric devices, ANSYS software facilitates the implementation of FEM to model and simulate thermoelectric behavior. The software enables coupling of thermal, and electrical properties, which are essential for an accurate representation of thermoelectric phenomena. In this subsection, we discuss the coupled equations used in the ANSYS software to model thermoelectric devices and their implications.

2.2.1. *Governing equations*

The governing equations for thermoelectric phenomena are the energy, electric potential, and current density equations are presented in this section.

2.2.1.1. Energy equation. The energy equation accounts for heat conduction, Joule heating, and the Thomson effect in the thermoelectric materials. The governing energy equations for the i^{th} component, *p*- and *n*-type thermoelectric pins, and alumina plates can be represented as follows in Equation *(1)*:

$$\nabla \bullet (k_i \nabla T) + \rho_i J^2 = \tau_i \vec{J} \bullet \nabla T \tag{1}$$

Here, τ denotes the Thomson coefficient, ρ represents the electrical resistivity, k refers to the thermal conductivity, and $\vec{J}$ signifies the local current density.

The left-hand side of Eq. *(1)* encompasses three terms: Fourier heat conduction and Joule resistive heating, while the right-hand side corresponds to the Thomson effect. For insulating alumina plates, the current generation density, J equals 0. The Thomson coefficient, τ, can be determined from the Seebeck coefficient using Equation *(2)*:

$$\tau_i = T\left(\frac{dS_i}{dT}\right) \tag{2}$$

In equation *(2)*, S is the Seebeck coefficient. When the Seebeck coefficient is temperature-independent, the Thomson coefficient is zero, and the Thomson effect can be disregarded. However, previous research has indicated that neglecting the Thomson effect results in an erroneous TEG power generation Zhang et al. [30]. In the current model, the Seebeck coefficient is temperature-dependent, and the Thomson effect is considered to ensure accuracy and reliability.

2.2.1.2. Electric potential equation. The movement of holes and electrons in semiconductors is driven by the electric potential field, and the governing equation for the electric potential field is given as [26]:

$$\nabla \bullet \left(\frac{\nabla \phi}{\rho_i}\right) = \nabla \bullet \left(\frac{S_i \nabla T}{\rho_i}\right) \tag{3}$$

Upon solving the electric potential, the electric potential of the electric field can be acquired as follows:

$$\vec{E} = -\nabla \phi + S_i \nabla T \tag{4}$$

2.2.1.3. Current density equation. The current density can be calculated using the electric field (E), which is derived from the electric potential and the electrical resistivity as follows [31]:

$$\vec{J} = \frac{\vec{E}}{\rho_i} \tag{5}$$

2.2.2. *Coupling of equations*

Equations *(1)*–*(5)* above are strongly coupled due to the interdependence of temperature, electric potential, and current density. The FEM in ANSYS software allows for simultaneous solving of these coupled equations, providing accurate results for the thermoelectric behavior.

2.2.3. *Boundary conditions*

In a broader context, when employing solar energy as the driving heat source for TEGs, sunlight is typically concentrated using an

Table 1
Mathematical expressions for the thermoelectric semiconductors [37].

Property	Expression
Seebeck coefficient (VK^{-1})	
p-BiTe	$-2.24407 \times 10^{-11}T^3 + 2.22834 \text{ x } 10^{-8}T^2 - 7.301 \text{ x } 10^{-6}T + 1.023898 \times 10^{-3}$
n-BiTe	$1.68178 \times 10^{-11}T^3 - 1.77163 \text{ x } 10^{-8}T^2 + 6.203 \text{ x } 10^{-6}T - 9.54589 \times 10^{-4}$
p-SKT	$8.8139 \times 10^{-5} - 3.6827 \times 10^{-10}T + 5.5507 \times 10^{-10}T^2 - 5.0917 \times 10^{-13}T^3$
n-SKT	$-7.2398 \times 10^{-5} - 2.7340 \text{ x } 10^{-7}T + 2.4331 \times 10^{-10}T^2 + 1.4197 \times 10^{-13}T^3$
Electrical resistivity (Ω-m)	
p-BiTe	$-7.75456 \times 10^{-13}T^3 + 7.77051 \times 10^{-10}T^2 - 0.01853 \text{ x } 10^{-5}T + 1.60117 \times 10^{-5}$
n-BiTe	$-6.04782 \times 10^{-13}T^3 + 6.09155 \times 10^{-10}T^2 - 1.715 \text{ x } 10^{-7}T + 2.11951 \times 10^{-5}$
p-SKT	$6.5155 \times 10^{-6} - 2.3672 \text{ x } 10^{-9}T + 2.6624 \times 10^{-11}T^2 - 2.0732 \times 10^{-14}T^3$
n-SKT	$2.9221 \times 10^{-6} + 1.5542 \text{ x } 10^{-8}T - 4.7078 \times 10^{-12}T^2 - 4.1703 \times 10^{-15}T^3$
Thermal conductivity ($Wm^{-1}K^{-1}$)	
p-BiTe	$-5.82609 \text{ x } 10^{-8}T^3 + 1.03491 \text{ x } 10^{-4}T^2 - 0.05011T + 8.726$
n-BiTe	$3.76869 \text{ x } 10^{-9}T^3 + 2.81722 \text{ x } 10^{-5}T^2 - 0.02057T + 5.09531$
p-SKT	$-2.0660 + 1.6390 \text{ x } 10^{-2}T - 2.4031 \text{ x } 10^{-5}T^2 + 1.2202 \text{ x } 10^{-8}T^3$
n-SKT	$1.4464 + 3.0553 \text{ x } 10^{-3}T - 4.4576 \text{ x } 10^{-6}T^2 + 2.4360 \text{ x } 10^{-9}T^3$
Dimensionless figure of merit	
p-BiTe	${S_{pc}}^2T/\rho_{pc}k_{pc}$
n-BiTe	${S_{nc}}^2T/\rho_{nc}k_{nc}$
p-SKT	${S_{ph}}^2T/\rho_{ph}k_{ph}$
n-SKT	${S_{nh}}^2T/\rho_{nh}k_{nh}$

optical solar concentrator, for instance the compound parabolic concentrator. Subsequently, the concentrated light is absorbed by a specialized coating affixed to the hot end's ceramic plate like a selective surface absorber [32]. As a result, the heat flux on the ceramic plate at the hot end can be determined using the equation below:

$$Q_{in} = C_{opt}GA_{mod}\eta_{opt}\eta_a \tag{6}$$

Here, C_{opt} is the optical solar concentration ratio, G represents the solar irradiance, assumed as 1000 Wm^{-2} in accordance with the AM 1.5G conditions [33]. Additionally, η_{opt} and η_a denote the optical efficiency, and the absorption efficiency, assumed to be 0.8 and 0.96, respectively [34]. A_{mod} is the surface area of the module assumed to be 40 × 40 mm^2 [35].

The cooling of the lower ceramic plate, q_{out}, is maintained at a constant cold junction convective film coefficient, $h_{conv,c}$, of 0.5 $kWm^{-2}K^{-1}$, operated at T_{film} and the corresponding cold junction temperature, T_c, is numerically determined. In this way, the cooling effect of the cold junction is quantified using the expression:

$$q_{out} = h_{conv,c}\left(T_c - T_{film}\right) \tag{7}$$

Furthermore, the upper ceramic plate is defined by a uniform hot junction convective film coefficient calculated using the McAdam's correlation, as suggested by Notton et al. [36], for flat surfaces exposed to outdoor wind conditions:

$$h_{conv,h} = 5.82 + 4.07w \tag{8}$$

where w is the wind speed assumed to be 1 m/s.

In terms of electrical boundary conditions, the TEG is linked to an external load, creating a closed circuit. Consequently, no current flows through the outer surfaces. Adiabatic boundary conditions are enforced on the TEG's external surfaces. It is assumed that temperature, heat flux, electric current, and electric potential exhibit continuity across the interfaces between distinct materials. Additionally, both electrical and thermal contact resistances are disregarded in this analysis.

2.3. Material properties

The material properties of the four thermoelectric semiconductors (BiTe-bismuth telluride and SKT-skutterudite) used in this work are provided in Table 1. The upper and lower ceramic plates are made of 96 % alumina while the metallic conductors that transfer current throughout the module are made of copper. The copper conductor is connected to the semiconductor using the solder interconnecting material. The thermal conductivity of the alumina, copper, and solder interconnection materials are specified as 25 $Wm^{-1}K^{-1}$, 401 $Wm^{-1}K^{-1}$, and 37.8 $Wm^{-1}K^{-1}$, respectively. The electrical resistivity of the copper and solder materials are 172 $\mu\Omega$-m and 500 $\mu\Omega$-m, respectively.

2.3.1. Performance parameters

The power output (P_{te}), thermoelectric efficiency (η_{te}), energy efficiency (η_{en}), exergy efficiency (η_{ex}), exergy input (Ex_{in}), exergy destruction (Ex_d), and entropy generation (S_{gen}) are defined as:

$$P_{te} = Q_h - Q_c \tag{9}$$

Table 2
Parameter ranges and constants [38,39].

S/N	Parameter	Range	Constant	Units
1.	C_{opt}	25–161	25	–
2.	$h_{conv,c}$	0.2–3	0.5	$kWm^{-2}K^{-1}$
3.	$h_{conv,h}$	7.85-26.17	9.89	$Wm^{-2}K^{-1}$
4.	T_a	273–315	295.15	K
5.	H_{te}	0.2–14.2	1.62	mm
6.	A_{te}	0.04-2.56	1.96	mm^2
7.	$\%SKT$	6.17–92.59	50	%

Table 3
Mesh refinement results

Case	Mesh element size (mm)	Grid nodes	Mesh elements	Energy efficiency (%)	Relative error (%)
1.	0.2	2436205	455950	0.808772881	0.00019041
2.	0.28	1094292	186683	0.808771341	0.00117439
3.	0.36	651089	107412	0.808761843	0.0052389
4.	0.44	415302	58652	0.808719475	0.15003903
5.	0.52	297645	40809	0.807507898	0.0243792
6.	0.6	247585	32506	0.807311082	0.00200588
7.	0.68	222662	28211	0.807327276	0.16808078
8.	0.76	151243	18771	0.805972591	0.06143783
9.	0.84	119418	12014	0.805477723	0.14794741
10.	0.92	98927	9244	0.8042878	–

$$\eta_{te} = \frac{P_{te}}{Q_h} \tag{10}$$

$$\eta_{en} = \frac{P_{te}}{Q_{in}} \tag{11}$$

$$\eta_{ex} = \frac{P_{te}}{Ex_{in}} \tag{12}$$

$$Ex_{in} = Q_{in}\left[1 - \frac{4}{3}\left(\frac{T_a}{T_s}\right) + \frac{1}{3}\left(\frac{T_a}{T_s}\right)^4\right] \tag{13}$$

$$Ex_d = Ex_{in} - P_{te} \tag{14}$$

$$S_{gen} = \frac{Ex_d}{T_a} \tag{15}$$

From Equations (9)–(15), Q_h and Q_c represent the heat in and out of the TEG's hot and cold junctions, respectively. T_a is the ambient temperature (295.15 K) and T_s is the Sun temperature (5778 K).

2.4. Numerical dataset

In this investigation, the estimation of thermal and geometric parameters for the operation and design of SVAL TEGs was scrutinized. An extensive dataset, encompassing TEG performance metrics such as energy, exergy, and entropy, along with semiconductor geometry parameters, was generated from numerical simulations executed with ANSYS software. ANSYS is a renowned design software employed by thermoelectric manufacturing companies worldwide, known for its ability to optimize high-performing TEGs. Table 2 shows the ranges and constants of the input parameters studied during the numerical simulation. These parameters are selected to include both low and high applications. The exhaustive dataset, containing various operating thermal and geometric parameters corresponding to distinct TEG performance metrics.

2.5. Mesh refinement results

In this study, the mesh refinement analysis was executed using the coarse and fine mesh configurations available through the ANSYS coupled steady-state thermal-electrical interface. The mesh quality relied on the element size, which was parametrically adjusted from 0.92 mm (coarse) to 0.2 mm (fine). Table 3 presents the results of the mesh refinement analysis. For every element size, the associated quantity of grid nodes and mesh elements were computed, and the impact of mesh quality on the system's energy efficiency was qualitatively examined.

The results in Table 3 reveal that enhancing mesh quality leads to an increased count of grid nodes and mesh elements. Specifically, the coarse mesh generates 98,927 grid nodes and 9244 mesh elements, whereas the fine mesh configuration results in 2,436,205 grid

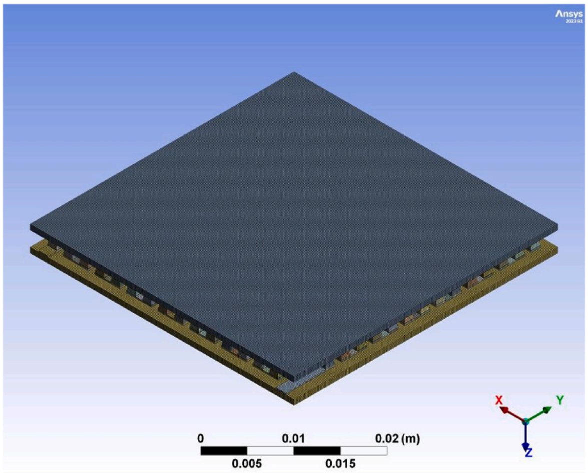

Fig. 2. Fine mesh resolution.

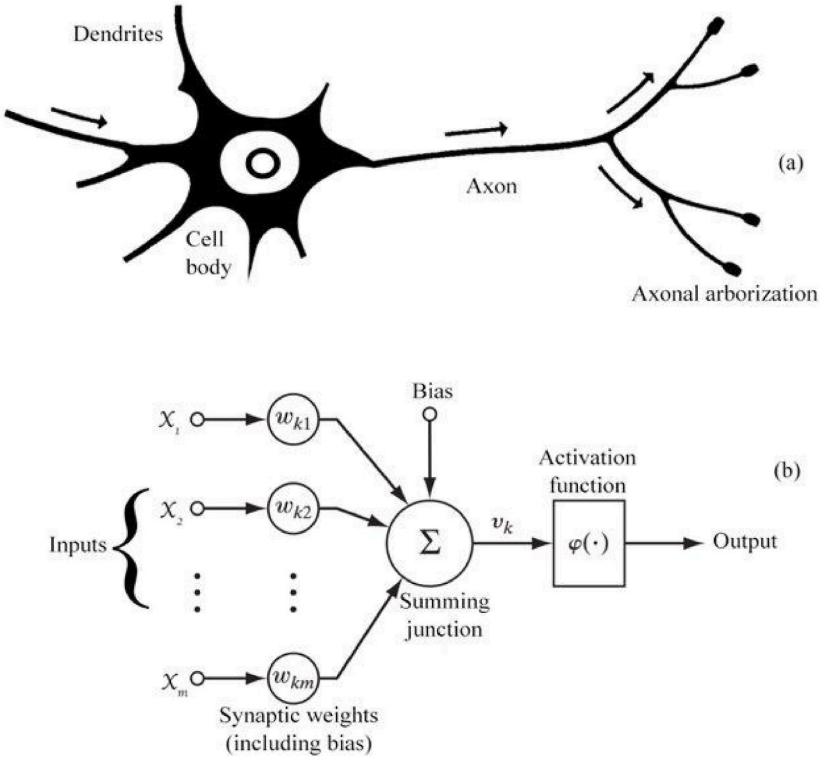

Fig. 3. Resemblances between the ANN and biological neurons.

nodes and 455,950 mesh elements, representing 25- and 49-times growth in the number of nodes and elements, respectively. In general, improving mesh quality implies heightened numerical precision at the cost of computational simplicity. Nonetheless, to guarantee numerical accuracy, the independence of the system's energy efficiency on the grid nodes must be confirmed.

Table 3 demonstrates that the system's efficiency ranges from 0.804 to 0.808 %, respectively. However, it converges at the fine mesh, as the relative error is the lowest, $\approx 1.9 \times 10^{-4}$. Consequently, the fine mesh configuration, as depicted in Fig. 2, is considered the optimal mesh resolution for the numerical optimization approach.

2.6. Neural network hyperparameters

The numerical model used to optimize the performance of thermoelectric modules is typically complex and time-consuming due to factors such as the three-dimensional digital twin considered, the numerous thermocouples in the full-scale module, the temperature

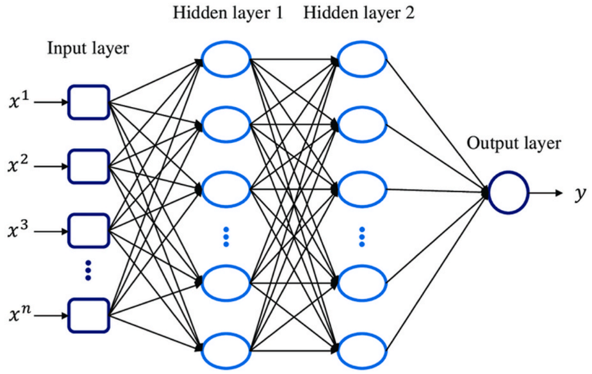

Fig. 4. Multilayer perceptron architecture diagram.

sensitivity of the semiconductors, and the diverse operating conditions evaluated. Furthermore, the high-resolution meshing of the 127 thermocouples (254 thermoelements) in three dimensions is computationally expensive and complex to solve. Researchers have found that combining numerical methods with neural networks can save considerable computational time and energy. In this section, we examine the performance of an ANN developed using three different training algorithms: Bayesian regularization (BR), Levenberg-Marquardt (LM), and scaled conjugate gradient (SCG). The ANNs were constructed with one hidden layer, ten neurons in the hidden layer by default, and the tansig activation function was employed to transmit signals between nodes. The numerical data was divided into 70 % for training, 15 % for testing, and 15 % for validation (for the BR ANN, it was 70 % for training, and 30 % for testing). The ANN consists of seven input nodes (representing the seven geometry and thermal parameters) and seven output nodes (representing the seven performance parameters investigated in this study).

2.6.1. *Artificial neural network*

Artificial neural networks have gained significant popularity in addressing various challenges across numerous fields. As a machine learning technique, ANNs are designed to mimic the functionality of the human brain and biological systems. A key strength of ANNs lies in their ability to generalize effectively, meaning they can produce accurate outputs based on inputs that were not encountered during the training process. This quality has made ANNs particularly valuable in solving issues related to thermoelectric module design in the energy industry.

2.6.2. *Neurons*

An ANN neuron's schematic representation and its similarities with a biological neuron is depicted in Fig. 3, which includes input signals, synaptic weights, an adder for aggregating the inputs, an activation function, and an output. This structure can be represented mathematically, as demonstrated in equations *16* and *17* [40].

Equation *(16)* represents the weighted sum of the inputs and bias

$$v_k = \sum_{i=1}^{N} (w_i x_i) + b_k \tag{16}$$

where: v_k = weighted sum of the inputs, w_i = weight associated with input i, x_i = input signal i, and b_k = bias term. N is the dataset size.

Equation *(17)* represents the output of the neuron after applying the activation function:

$$y = \phi(v_k) \tag{17}$$

2.6.3. *Activation function*

The various activation functions employed in neurons serve distinct purposes and are selected based on the specific requirements of the problem being addressed. Commonly used activation functions include Gaussian, sigmoid, and linear functions, among others. The sigmoid function, which is frequently utilized due to its versatile nature, can be represented mathematically as shown in Equation *(18)* [41]:

$$\phi(v_k) = (1 + exp(-v_k))^{-1} \tag{18}$$

where: $\phi(v_k)$ = output of the sigmoid activation function, v_k = weighted sum of the inputs and bias.

2.6.4. *Multilayer perceptron architecture*

In this study, the ANN model employed is the multilayer perceptron (MLP) model, which is widely used in various applications due to its ability to model complex relationships in data. The MLP neural network is composed of an input layer, one or more hidden layers, and an output layer. A schematic representation of a typical MLP neural network can be seen in Fig. 4 which illustrates the arrangement of layers and their interconnections, emphasizing the hierarchical structure that characterizes this type of network.

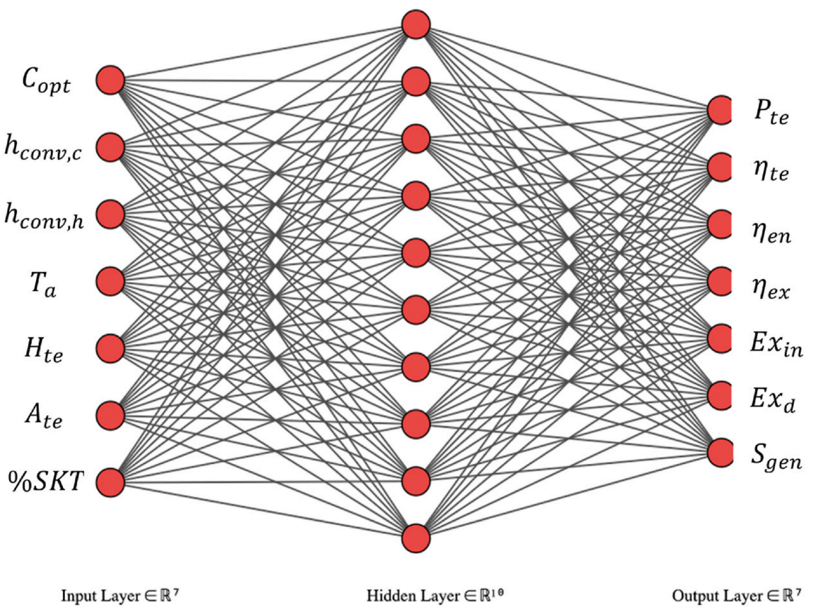

Fig. 5. Artificial neural network model studied in this work.

2.6.5. Backpropagation algorithm

The backpropagation algorithm is used to train MLP neural networks, which involves adjusting the weights and biases during the learning process to ensure that the network produces the desired output. There are several training algorithms available, such as Levenberg-Marquardt, Gradient Descent, Newton, Scaled Conjugate Gradient, and Quasi-Newton. In this study, the Bayesian Regularization neural network was employed, and its performance was compared to that of the LM and SCG algorithms.

2.6.5.1. Levenberg-Marquardt algorithm. The LM algorithm is an optimization method that combines the advantages of Gradient Descent and the Gauss-Newton algorithm. LM is particularly suitable for training small to medium-sized neural networks because it offers faster convergence and is less prone to getting stuck in local minima. However, it requires more memory and computational resources than other algorithms.

The governing equation for the LM algorithm can be written as [42]:

$$(W+\lambda I)\Delta W = -G(W) \tag{19}$$

where W represents the vector of weights and biases, λ is a damping factor, I is the identity matrix, $G(W)$ is the gradient of the error function with respect to W, and ΔW is the update vector for the weights and biases. The damping factor, λ, is adjusted during the training process. If the error decreases, λ is reduced, making the algorithm behave more like the Gauss-Newton method. If the error increases, λ is increased, causing the algorithm to behave more like Gradient Descent. This adaptive behavior allows for faster convergence and improved robustness compared to Gradient Descent alone.

2.6.5.2. Scaled conjugate gradient algorithm. The SCG algorithm is an improvement of the Conjugate Gradient algorithm, which aims to adapt the step size, α, and the conjugate gradient update parameter, β, to optimize the convergence rate. The governing equations for the SCG algorithm include the weight update equation and the search direction update equation, like the Conjugate Gradient algorithm. The governing equation for the CG algorithm can be expressed as Hestenes and Stiefel [43]:

$$\Delta W = \alpha P \tag{20}$$

where ΔW is the update vector for the weights and biases, α is the step size, and P is the search direction vector. The search direction vector, P, is updated as follows [44]:

$$P_{new} = -G(W) + \beta P_{old} \tag{21}$$

where $G(W)$ is the gradient of the error function with respect to W, and β is a scalar value calculated using several formulas, such as the Hestenes-Stiefel formula. The SCG algorithm adjusts α and β at each iteration by performing a line search to find the optimal values for these parameters, which in turn leads to an accelerated convergence rate compared to the standard CG algorithm. The line search is typically performed using a combination of quadratic and cubic interpolations to estimate the optimal step size.

2.6.5.3. Bayesian Regularization Algorithm. The BR algorithm is a training function that updates the weights and biases based on the LM algorithm while introducing a regularization term to prevent overfitting. It offers strong generalization capabilities for small datasets and helps to address overfitting issues. This makes BR an effective choice for training neural networks in situations where data

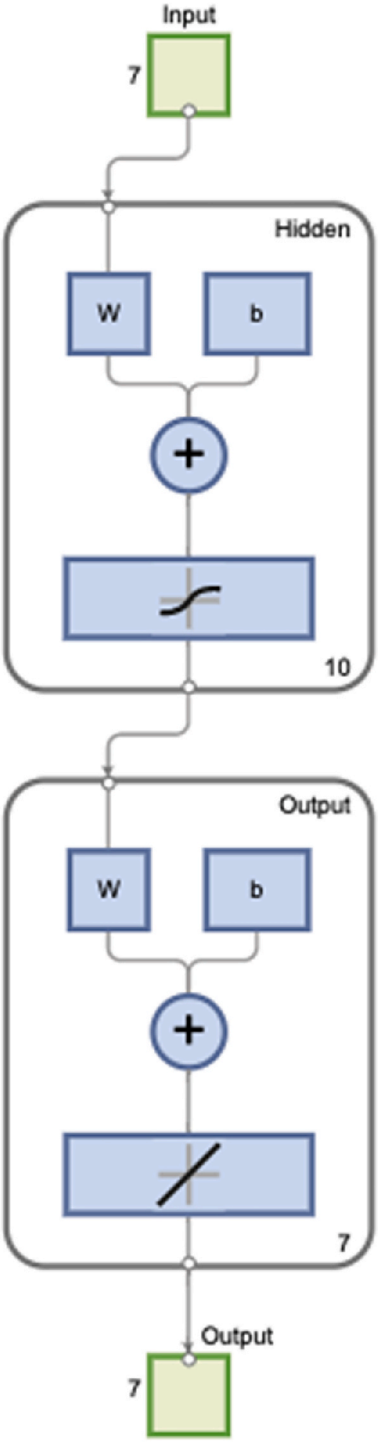

Fig. 6. Neural network diagram used for the TEG performance parameters prediction.

is limited, or overfitting is a concern. The BR algorithm was developed by MacKay in his seminal work [45] which introduced a Bayesian approach to training artificial neural networks, which helped mitigate overfitting and improve generalization, especially when dealing with small datasets. The governing equation for the BR algorithm can be written as [45]:

$$(W + \lambda I + \alpha I)\Delta W = -G(W) \tag{22}$$

where W represents the vector of weights and biases, λ is a damping factor, α is the regularization parameter, I is the identity matrix,

$G(W)$ is the gradient of the error function with respect to W, and ΔW is the update vector for the weights and biases. The BR algorithm estimates the hyperparameters λ and α during the training process using the evidence maximization/empirical Bayes/Type-II maximum likelihood approach. This allows the algorithm to balance the trade-off between fitting the data and maintaining a simple model, leading to better generalization performance, especially when dealing with small or noisy datasets.

2.7. *Artificial neural network model description*

In this study, MLP neural network is employed to forecast the energy, exergy, and entropy performance of a solar thermoelectric generator, with the model developed in MATLAB. The MLP features three layers: an input layer with seven neurons representing the solar concentration ratio, cold junction cooling coefficient, hot junction convective coefficient, ambient temperature, semiconductor height, semiconductor cross-sectional area, and percentage skutterudite content, all of which were acquired from numerical simulations used in the thermoelectric design process in the manufacturing sector. Additionally, the model includes a single hidden layer containing ten neurons, selected through a parametric analysis, and an output layer with seven neurons corresponding to the desired performance indicators. These indicators encompass power output, thermoelectric efficiency, energy efficiency, exergy efficiency, exergy input, exergy destruction, and entropy generation. Fig. 5 illustrates the ANN model implemented in this research, while Fig. 6 displays the network diagram for the neural network employed in predicting the performance parameters for the TEG manufacturing process.

2.7.1. *Bayesian model Theory*

Artificial neural networks can sometimes encounter issues related to overfitting or underfitting. The overfitting issue is particularly concerning, as it can result in predictions that fall outside the scope of the training dataset. Overfitting typically arises when a network model accurately fits the training data, which in turn leads to a substantial generalization error. To mitigate overfitting problems, Bayesian regularization can be employed. This approach involves modifying the early stopping objective function which measures the error between the target outputs and the predicted outputs for the training dataset, as represented in equation *(23)* [46].

$$E(D \mid w, M) = \sum (y_i - y_i')^2 \tag{23}$$

where $D = \{y, (p_i)\}$ for $i = 1$ to N, E is the error function, D represents the training dataset, w is the weights, M is the model complexity, y_i is the target output, and y_i' is the predicted output for the i^{th} data point. To further improve the performance of the ANN and prevent overfitting, Bayesian regularization can be applied. In Bayesian regularization, an additional term is included in the objective function [47]:

$$E_{reg}(D \mid w, M) = E(D \mid w, M) + \lambda R(w) \tag{24}$$

In equation *(24)*, E_{reg} is the regularized error function, and $R(w)$ is a regularization term that penalizes large weights in the network, which can lead to overfitting. In many cases, large weights can cause the network to fit the training data very closely, capturing noise and inconsistencies, which in turn reduces the network's ability to generalize to new, unseen data. The regularization term is designed to add a penalty for large weights, effectively encouraging the network to find a simpler model with smaller weights that can still fit the data well. There are different types of regularization terms used in machine learning, with two common ones being $L1$ and $L2$ regularization. In $L2$ regularization, $R(w)$ is defined as the sum of the squares of all the weights in the network:

$$R(w) = \sum_{i=1}^{N} w_i^2 \tag{25}$$

where N is the total number of weights in the network and w_i is the i^{th} weight. The parameter, λ, is a regularization coefficient that controls the trade-off between minimizing the error and preventing overfitting by penalizing large weights. When λ is small, the network's focus is primarily on minimizing the error on the training data, which can lead to overfitting. Conversely, when λ is large, the network is more focused on minimizing the size of the weights, which can result in underfitting. Therefore, choosing the right value for λ is crucial for achieving the best trade-off between fitting the training data accurately and maintaining good generalization performance on new, unseen data. In practice, the optimal value for λ can be determined through techniques such as cross-validation, where different values of λ are tested on different subsets of the data, and the one that yields the best generalization performance is chosen. By minimizing the regularized error function (E_{reg}), the ANN can achieve a balance between fitting the training data accurately and maintaining good generalization performance on new, unseen data.

Recall that the Levenberg-Marquardt optimization modifies the Gauss-Newton algorithm, as shown in equation *(26)* [48]:

$$(\lambda I)\delta = J^T e \tag{26}$$

Here, the Hessian matrix is approximated as:

$$H = J^T J \tag{27}$$

In equation *(27)*, J represents the Jacobian matrix, λ is the Levenberg damping factor, δ is the parameter update vector and e is the error vector used to guide the adjustments made to the weights and biases during the training process, aiming to minimize the error and improve the overall performance of the neural network. The parameter update vector signifies the extent to which the weight values

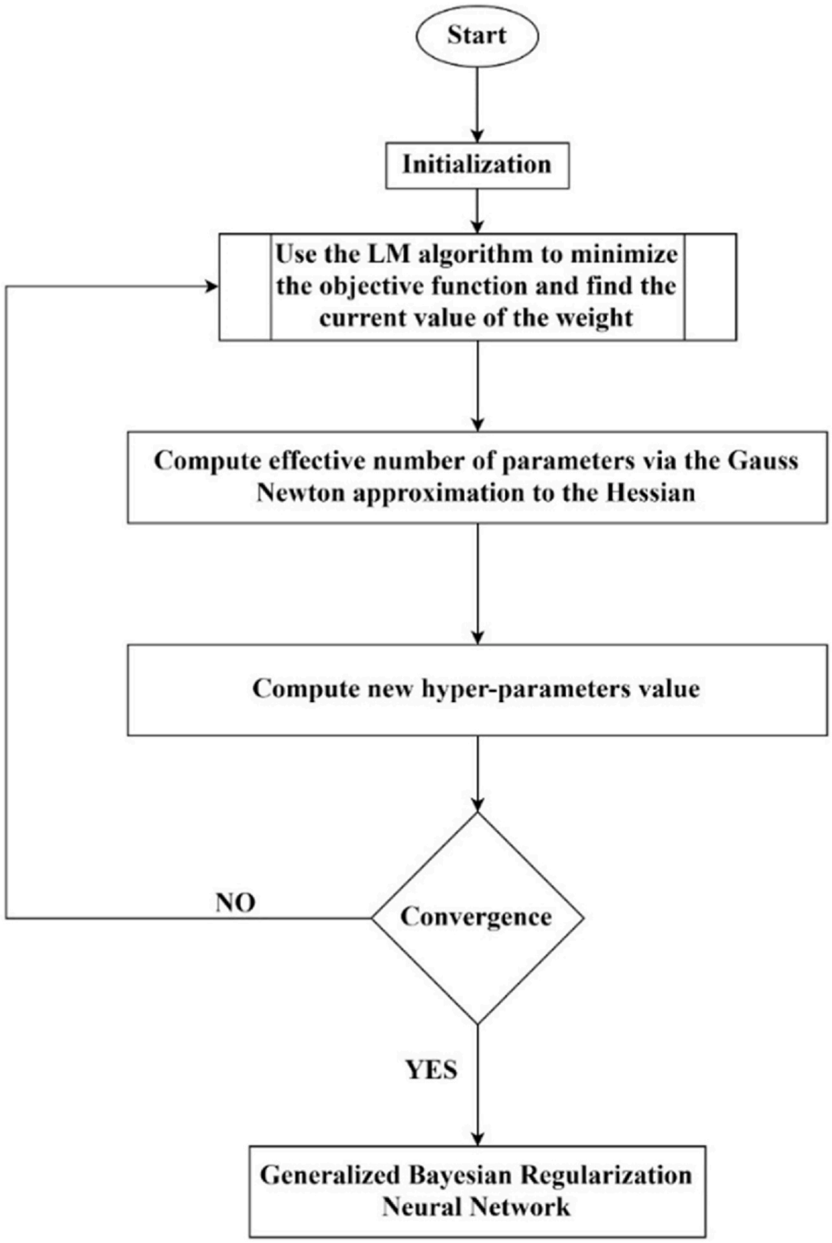

Fig. 7. Flow chart of Artificial Neural Network with the Bayesian Regularization Algorithm.

should be adjusted to improve the prediction accuracy. The Jacobian matrix (the partial derivative of the output with respect to the weight) J is defined as [49]:

$$J=\left[\frac{\partial e_1(w)}{\partial w_1}\ \frac{\partial e_1(w)}{\partial w_2}\ \cdots\ \frac{\partial e_1(w)}{\partial w_n}\ \frac{\partial e_2(w)}{\partial w_1}\ \frac{\partial e_2(w)}{\partial w_2}\ \cdots\ \frac{\partial e_2(w)}{\partial w_n} \vdots \vdots \ddots \vdots \frac{\partial e_N(w)}{\partial w_1}\ \frac{\partial e_N(w)}{\partial w_2}\ \cdots\ \frac{\partial e_N(w)}{\partial w_n}\right] \tag{28}$$

The stepwise algorithm for Bayesian regularization adjusts the weights and hyperparameters iteratively until convergence is reached as shown in Fig. 7. It involves updating the posterior distribution of the weights based on the evidence maximization approach. This modification of the standard backpropagation algorithm helps improve the performance of the neural network and avoid issues such as overfitting.

The methodology of the BNN deployed, its neural architecture and hyperparameter tuning process has been included in the supplementary data file.

The Bayesian Neural Networks have been as against other machine learning models because of the following reasons.

i. *Robust Generalization:* BNNs offer strong generalization capabilities, which is crucial for predicting thermoelectric generator performance under various operating conditions. This is particularly important given the complex nature of the TEG systems and the diversity of the data.
ii. *Handling Uncertainty:* BNNs are adept at managing uncertainties in the data. The Bayesian approach allows the model to quantify uncertainty in its predictions, which enhances the reliability of the results. This is particularly beneficial when dealing with small or noisy datasets, as is often the case in real-world applications.
iii. *Prevention of Overfitting:* The Bayesian Regularization approach mitigates overfitting by introducing a regularization term. This is especially important for our study, where the dataset, while comprehensive, might still pose risks of overfitting due to its complexity and size.
iv. *Computational Efficiency:* While BNNs can be computationally intensive, the balance they strike between computational demands and prediction accuracy makes them suitable for our study. The trade-off is managed efficiently through the use of robust training algorithms like the Levenberg-Marquardt and Scaled Conjugate Gradient methods, which optimize the convergence rate.
V. *Model Complexity and Interpretability*: BNNs provide a good balance between model complexity and interpretability. They are sufficiently complex to capture the intricate relationships within the data but remain interpretable enough to provide insights into the model's workings and outputs.

2.8. *Performance metrics evaluation*

Evaluating the performance of a neural network model is essential to ensure its reliability and precision. A variety of performance metrics can be applied, including mean square error (MSE), mean relative error, mean absolute error, and mean accuracy percentage error. In this study, the mean squared error (MSE) and coefficient of determination (R^2) were selected as performance metrics.

The mathematical expression for the MSE is given by Equation *(29)*:

$$MSE = \left(\frac{1}{N}\right) \sum_{i=1}^{N} \left(y_i - y_i'\right)^2 \tag{29}$$

where N is the number of observations, y_i is the actual value, and y_i' is the predicted value.

The coefficient of determination (R^2) is a measure that indicates the proportion of the variance in the dependent variable that is predictable from the independent variable(s). It is mathematically defined by Equation *(30)*:

$$R^2 = 1 - \left(\frac{\sum_{i=1}^{N} \left(y_i - y_i'\right)^2}{\sum_{i=1}^{N} \left(y_i - y_{mean}\right)^2}\right) \tag{30}$$

where y_{mean} is the mean of the actual values. The R^2 value ranges from 0 to 1, with a value closer to 1 indicating a better fit of the model to the data.

Finally, Equation *(31)* can be rewritten in terms of the MSE and total sum of squares (TSS) as:

$$R^2 = 1 - \left(\frac{N \times MSE}{TSS}\right) \tag{31}$$

where $TSS = \sum_{i=1}^{N} \left(y_i - y_{mean}\right)^2$. Finally, Equation *(32)* can be rewritten in terms of the residual sum of squares (RSS) as

$$R^2 = 1 - \frac{RSS}{TSS} \tag{32}$$

where $RSS = NMSE$.

2.9. *Computational capacity*

In this study, a computer equipped with an Intel(R) Core (TM) i5-8300H CPU @ 2.30 GHz processor, 32 GB of RAM, and running a 64-bit Windows Operating System was employed. The MATLAB software from MathWorks was utilized to construct the ANN model, leveraging built-in capabilities such as the neural network toolbox. The software offers an interactive graphical interface, as well as robust data plotting tools that enable customization of colors, sizes, and scales for optimal visualization.

2.10. *Computational demands and feasibility*

The advanced models employed in this study, including the three-dimensional digital twin and artificial neural networks, inherently demand significant computational resources. High-resolution meshing and complex simulations contribute to the overall computational load. For instance, the training phases of ANNs, particularly those utilizing algorithms such as Bayesian Regularization (BR), Levenberg-Marquardt (LM), and Scaled Conjugate Gradient (SCG), are computationally intensive due to their iterative nature and the need for large datasets.

Despite these demands, the choice of optimized algorithms like LM and SCG helps mitigate the computational load by facilitating

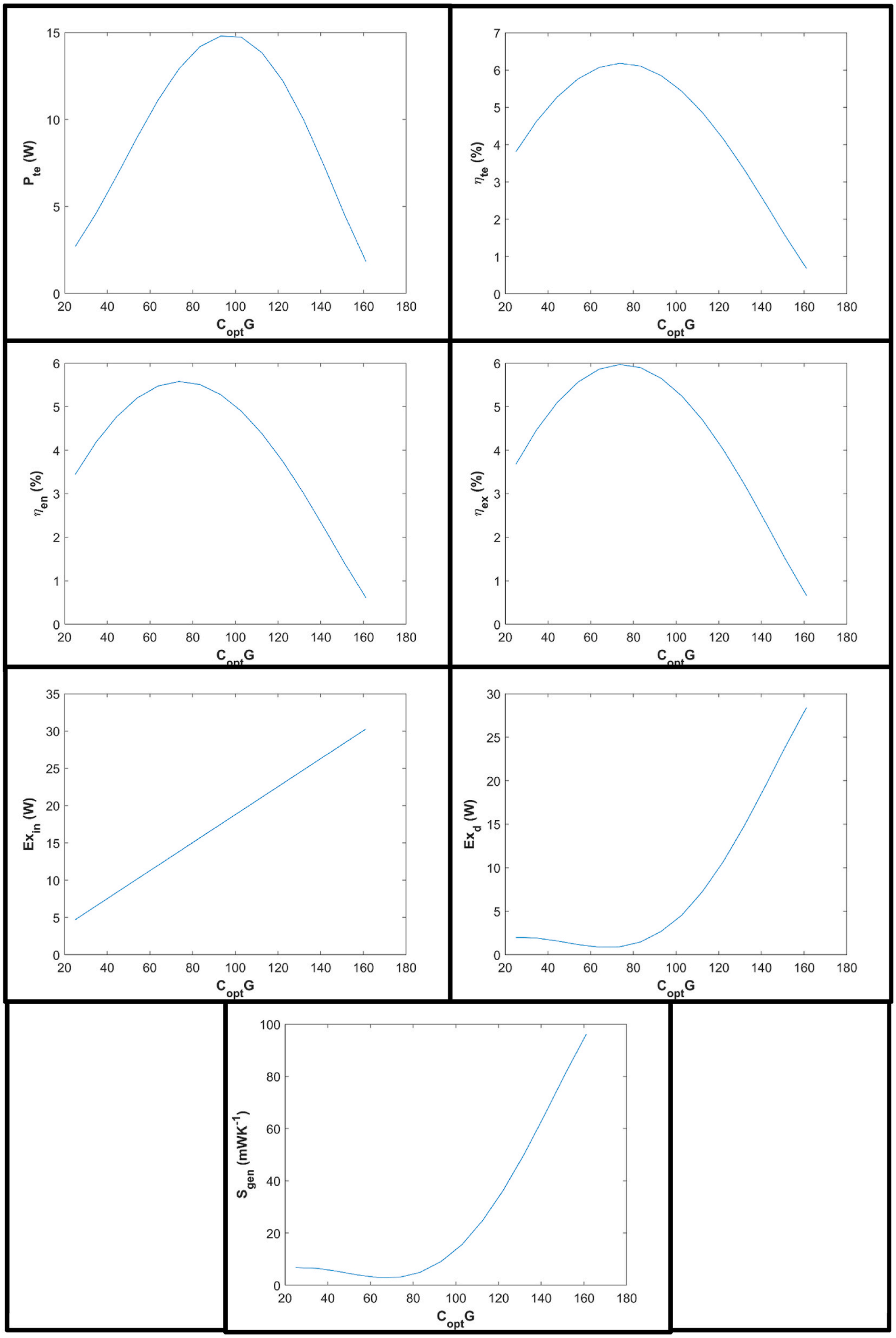

Fig. 8. Effect of the optical concentration ratio on the TE power output and conversion efficiency, energy efficiency, exergy efficiency, exergy input, exergy destruction rate, and entropy generation rate.

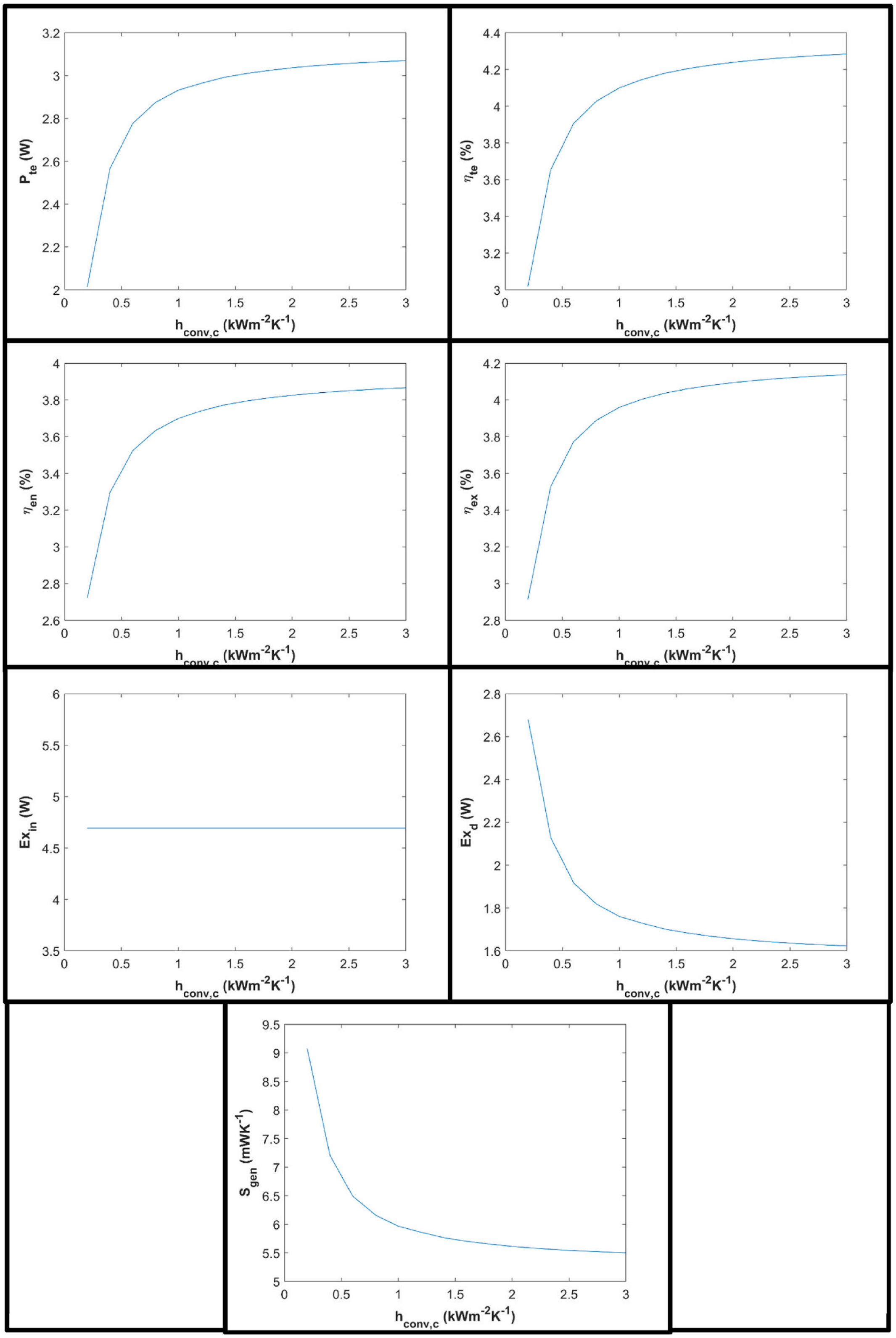

Fig. 9. Influence of the cold junction heat transfer coefficient on the TE power output and conversion efficiency, energy efficiency, exergy efficiency, exergy input, exergy destruction rate, and entropy generation rate.

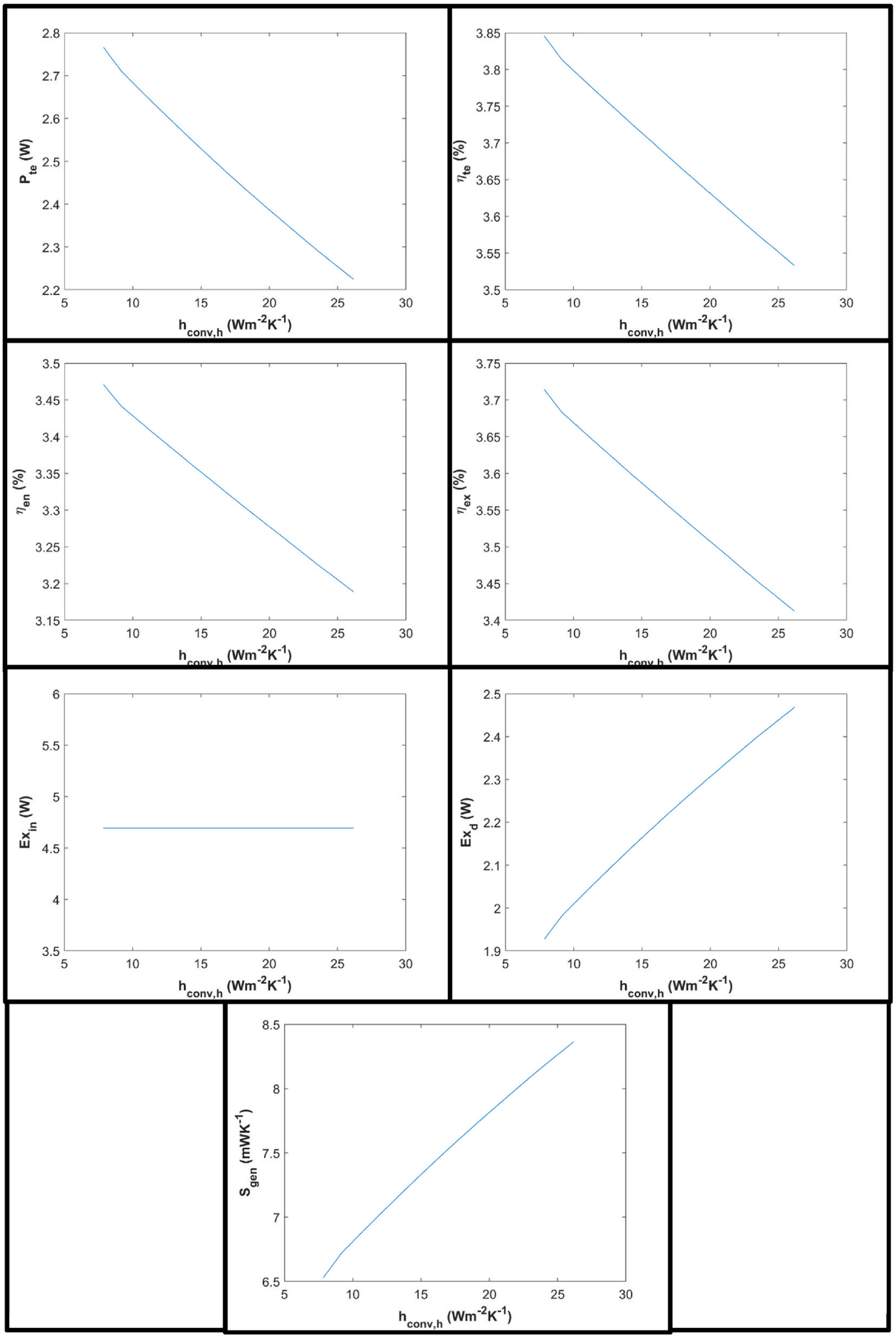

Fig. 10. Impact of the hot junction heat transfer coefficient on the TE power output and conversion efficiency, energy efficiency, exergy efficiency, exergy input, exergy destruction rate, and entropy generation rate.

faster convergence. In real-time scenarios, simplified versions of these models can be implemented. Modern hardware accelerators such as GPUs and TPUs can significantly enhance both training and inference speeds, making real-time applications more feasible.

For deployment on less capable hardware, techniques such as model pruning, quantization, and knowledge distillation can be employed to develop lightweight models that maintain high accuracy while reducing computational requirements. Cloud computing also presents a viable solution for offloading complex computations, allowing for resource-constrained devices to leverage powerful remote servers.

3. Results and discussions

In this segment, the outcomes derived from the numerical thermal and geometry optimization schemes by employing ANSYS software and the suggested neural network prediction of the device's performance are displayed. The substantiation of the numerical findings through a mesh refinement analysis and juxtaposition with published numerical and experimental outcomes is provided. Furthermore, the calculation of optimal geometry and thermal design parameters for attaining optimal energy, exergy, and entropy performances are demonstrated, along with the effectiveness of the present optimization approach in augmenting the device's performance.

3.1. Thermal parameters

The results of the thermal parameters on the power output (P_{te}), thermoelectric efficiency (η_{te}), exergy efficiency (η_{te}), exergy destruction (Ex_d), and entropy generation (S_{gen}) are presented in this section. The thermal parameters studied are the optical solar concentration ratio (C_{opt}), cold junction convective film coefficients ($h_{conv,c}$), hot junction convective film coefficients ($h_{conv,h}$), and air temperature (T_a).

3.1.1. Optical solar concentration ratio

In this study, the impact of the optical concentration ratio of a solar concentrator on the performance of a proposed thermoelectric device design is examined, as shown in Fig. 8. The thermoelectric power output, efficiency, and energy and exergy efficiencies are found to be optimized at different optical concentration ratios. The optical solar concentration ratio was varied from 25 to 161, while other boundary conditions were kept constant, to explore high and low solar concentration levels and identify the optimal points that maximize system performance.

The maximum power output of 14.8 W was achieved at an optical concentration ratio of 93. The highest thermoelectric, energy, and exergy efficiencies of 6.2 %, 5.6 %, and 6.0 %, respectively, were observed at a concentration ratio of 74. It was also noted that the exergy input into the system increased progressively as the solar concentrator's concentration ratio increased.

Initially, the exergy destruction and entropy generation remained nearly constant, but beyond a concentration ratio of 74, they exhibited exponential and then linear growth. The minimum value of the exergy destruction and entropy generation at this optimum solar concentration ratio are 0.9 W and 2.9 mWK^{-1}, respectively. This optimal value corresponds to the optical concentration ratio that yields maximum efficiency from the system. This finding is crucial, as it indicates that operating the system at the optimal solar concentration ratio for maximum efficiency leads to minimized exergy destruction and entropy generation only when the solar concentration ratio is varied.

3.1.2. Cold junction cooling

Fig. 9 illustrates the effects of the cold junction cooling coefficient on the performance parameters of the system. The cooling film coefficient was varied from 0.2 to 3 $kWm^{-2}K^{-1}$ while operating under a concentrated solar flux of 25 Suns and maintaining other boundary conditions constant to reflect low and high cooling conditions. The plot reveals that higher film coefficients positively impact the system's power and efficiencies.

More specifically, power and efficiency initially increase linearly for lower film coefficients, but the rate of increase diminishes as we approach higher film coefficients. For film coefficients ranging from 0.2 to 1 $kWm^{-2}K^{-1}$, the power output rises from 2.01 W to 2.93 W, representing a 45.61 % increase in the device's power production. However, for film coefficients between 2.2 and 3 $Wm^{-2}K^{-1}$, the power production only increases from 3.05 W to 3.07 W, a mere 0.79 % rise in the system's power. This finding supports the idea that as the film coefficient progressively increases, the cooling effect from the system's cold junction does not necessarily improve, due to the thermal resistivity of the cold junction of the device (alumina) limiting further heat transfer [50]. Hence, economic considerations should be considered when selecting the pump used to extract heat from the cold junction of the device to ensure proper cooling and enhanced system performance. Additionally, it was observed that the exergy input of the system remained constant for all heat transfer coefficients due to the imposed constant solar flux on the operating system. Finally, the entropy generation and exergy destruction rate of the system decrease exponentially as the film coefficient increases, which explains the rise in system power and efficiency.

3.1.3. Hot junction convective film coefficient

Fig. 10 illustrates the impact of the hot junction convective film coefficient on the overall performance of the system. In this study, the convective film coefficient was estimated using McAdam's correlation, as suggested by Duffie and Beckman in Notton et al. [36], for flat surfaces exposed to outdoor wind conditions. Wind speed was varied from 0.5 to 5 ms-1, representative of average South-Eastern Nigerian weather conditions, corresponding to film coefficients of 7.8–26.1 $Wm^{-2}K^{-1}$, respectively. Mathematical expressions were employed to estimate the convective film coefficient, which was then imposed on the three-dimensional numerical digital twin model created in ANSYS simulation software.

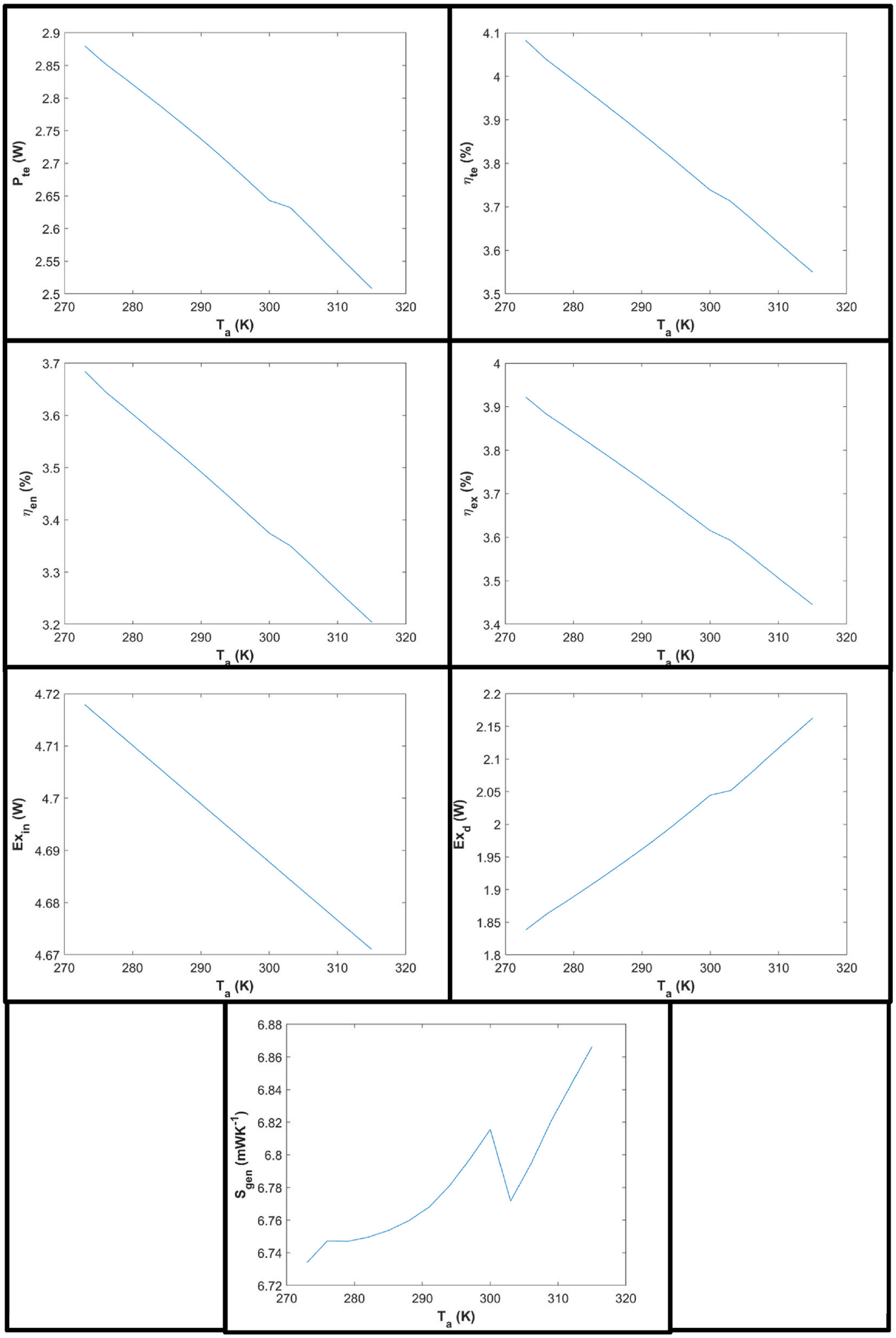

Fig. 11. Consequence of the air temperature on the TE power output and conversion efficiency, energy efficiency, exergy efficiency, exergy input, exergy destruction rate, and entropy generation rate.

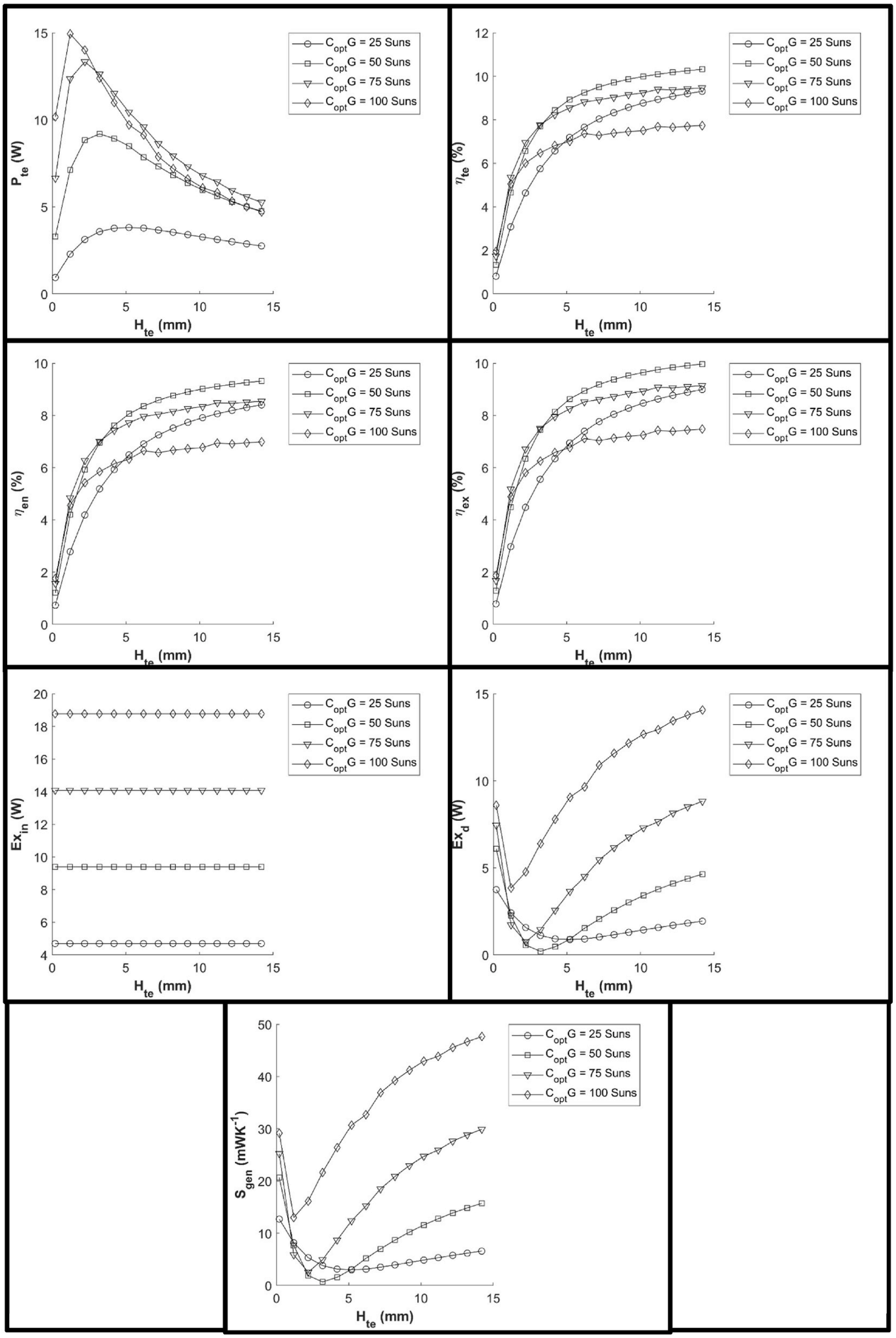

Fig. 12. Outcome of the semiconductor height on the TE power output and conversion efficiency, energy efficiency, exergy efficiency, exergy input, exergy destruction rate, and entropy generation rate.

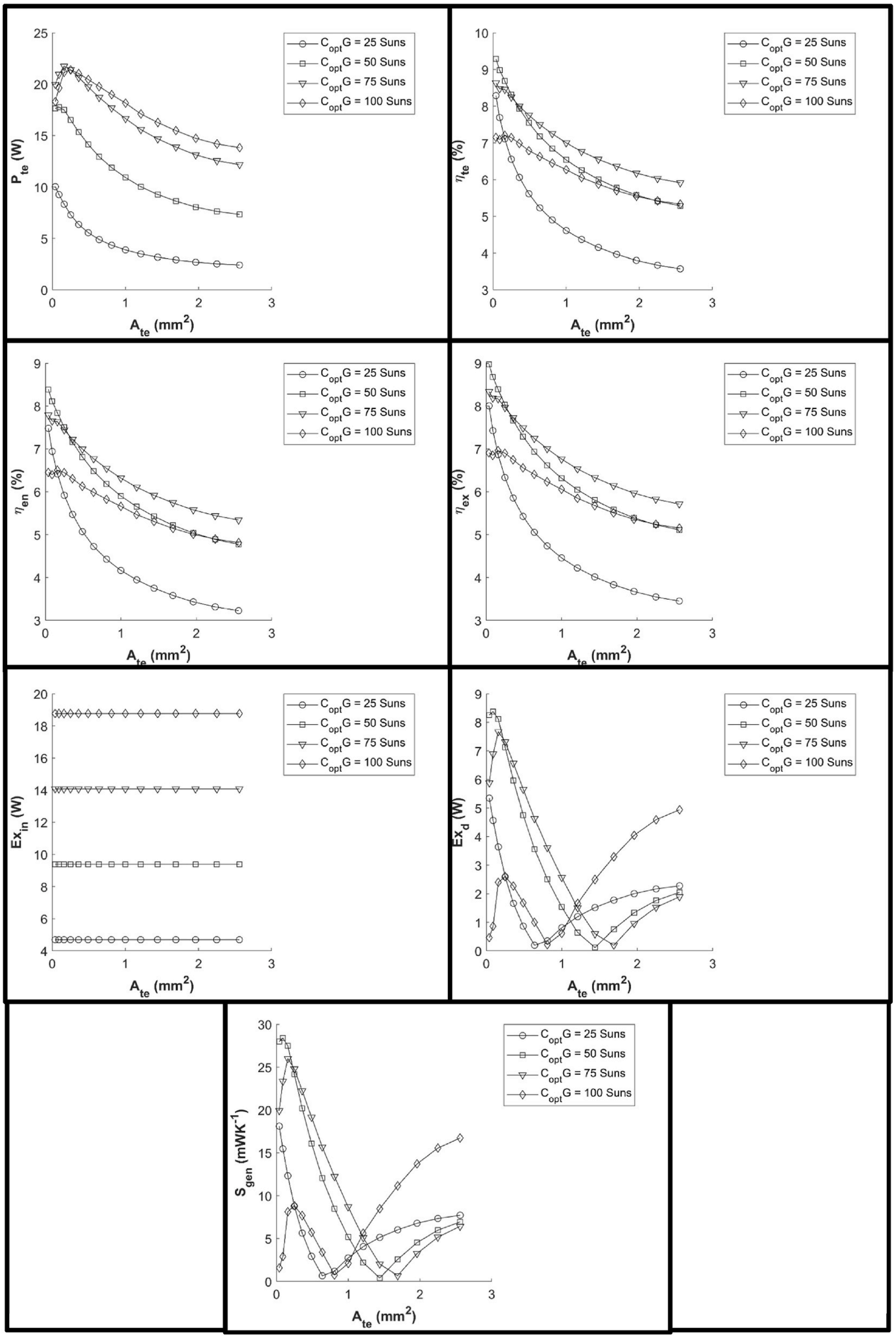

Fig. 13. Result of the semiconductor cross-sectional area on the TE power output and conversion efficiency, energy efficiency, exergy efficiency, exergy input, exergy destruction rate, and entropy generation rate.

The analysis demonstrates that higher convective film coefficients at the device's hot junction result in reduced system performance. This reduction is attributed to the smaller temperature gradient between the device's junctions, due to increased wind flow speeds at the top alumina plate. Consequently, the system's power output, thermoelectric efficiency, energy efficiency, and exergy efficiency decrease as the hot junction film coefficient increases. Moreover, the exergy input remains constant with increasing hot junction convective film coefficient, as the concentrated solar irradiance is effectively fixed.

To further understand the decline in system performance parameters with increasing hot junction convective heat transfer coefficient, it is observed that the exergy destruction rate and entropy generation of the system increase as the convective film coefficient rises. This growth in destroyed exergy and generated entropy is attributed to the higher irreversibility in the system as the hot junction film coefficient increases.

3.1.4. Air temperature

This study also considers the effects of ambient temperature on the proposed thermoelectric system as shown in Fig. 11. Ambient temperature was varied from 273 K to 315 K to account for both low and high temperature applications. Operating the system in a high temperature environment reduces its performance due to the added ambient heating, which increases both hot and cold junction temperatures, ultimately diminishing the temperature gradient and overall system performance. Conversely, operating the system in a colder environment does not contribute to heating the cold junction, resulting in a larger temperature gradient between the hot and cold junctions compared to a warmer environment.

Additionally, it is observed that the exergy input gradually decreases as the ambient temperature rises, in line with Petela's exergy expression [51]. The exergy destruction rate also increases with ambient temperature, which is expected since the system's performance parameters decline as the ambient temperature increases. Finally, the entropy generation rate decreases with ambient temperature. However, the range of variation in these parameters is relatively small (6.7–6.9 mWK^{-1}), as the exergy destruction is being divided by the ambient temperature.

3.2. Geometry parameters

Prior research on geometry optimization of segmented variable area leg thermoelectric generators operating under variable solar flux conditions focused on the impact of the thermoelectric geometry on system performance. However, these studies only analyzed a single thermoelectric couple consisting of one pair of *n*- and *p*-type semiconductors. This assumption overlooks the mutual interaction between all the thermocouples (typically 127) that make up an actual module. As a result, the temperature calculations derived from the numerical solver may be unreliable, and the optimization outcomes might lack practical feasibility.

3.2.1. Semiconductor height

In this study, Fig. 12 illustrates the impact of thermoelectric height on the output performance parameters of the thermoelectric module. It is observed that the thermoelectric power output (Watts) reaches its maximum at an optimal semiconductor height, which decreases as the concentrated solar flux increases. For instance, at concentrated solar irradiances of 25 Suns, 50 Suns, 75 Suns, and 100 Suns, optimal semiconductor heights of 5.2 mm, 3.2 mm, 2.2 mm, and 1.2 mm yield maximum power outputs of 3.8 W, 9.2 W, 13.3 W, and 14.9 W, respectively. This pattern further substantiates the notion that higher solar fluxes generate greater power outputs due to increased thermal energy absorption at the module's hot junction ceramic plate.

Regarding the three efficiency types (thermoelectric, energy, and exergy), using longer thermoelectric legs consistently increases efficiency values which agrees with the findings of previous researches in this area. Further analysis reveals that efficiency initially increases linearly; however, as the height continues to grow, the efficiency increase becomes more subdued, appearing nearly constant. As anticipated, the exergy input remains constant with an increase in thermoelectric height, although a higher concentrated solar flux results in greater exergy input into the system.

Moreover, the exergy destruction and entropy generation within the system are minimized at an optimal thermoelectric leg height, which aligns with the requirements for maximum power generation (Wattage). Both entropy generation and exergy destruction increase below and above this optimal thermoelectric height. Calculated data shows that concentrated solar fluxes of 25 Suns, 50 Suns, 75 Suns, and 100 Suns yield minimum exergy destruction rates (Watts) and entropy generation (mWK^{-1}) of 0.88 W and 3 mWK^{-1}, 0.2 W and 0.7 mWK^{-1}, 0.75 W and 2.5 mWK^{-1}, 3.8 W and 13 mWK^{-1}, respectively. This trend indicates that minimum exergy destruction and entropy generation increase as the concentrated solar flux appreciates, due to the rising amount of exergy inflow at the module's hot junction.

In summary, the optimal semiconductor height that maximizes the system's power output also minimizes the exergy destruction and entropy generation rates of the module. However, using longer thermoelectric semiconductors leads to an increase in the system's efficiencies.

3.2.2. Semiconductor cross-sectional area

This analysis investigates the effects of the thermoelectric cross-sectional area (achieved by altering the width of the four semiconductors) on the power, efficiency, and entropy of the thermoelectric module, as depicted in Fig. 13. Generally, the module's power and efficiency decrease as the cross-sectional area of the thermoelectric pins increases. This trend can be attributed to the so-called heat dissipation effect, which occurs as the width of the semiconductors increases, causing a reduction in the thermal gradient and subsequently a decline in the system's power and efficiency performance. However, this phenomenon is only observed for the power output when operated under low heat fluxes of 25 and 50 Suns. For higher heat fluxes of 75 and 100 Suns, the maximum power output is attained only at an optimum cross-sectional area of 0.16 mm^2, which generates the maximum power outputs of 21.8 W and 21.4 W, respectively. This result implies that the maximum power generation also has an optimal concentrated solar irradiance of 75 Suns

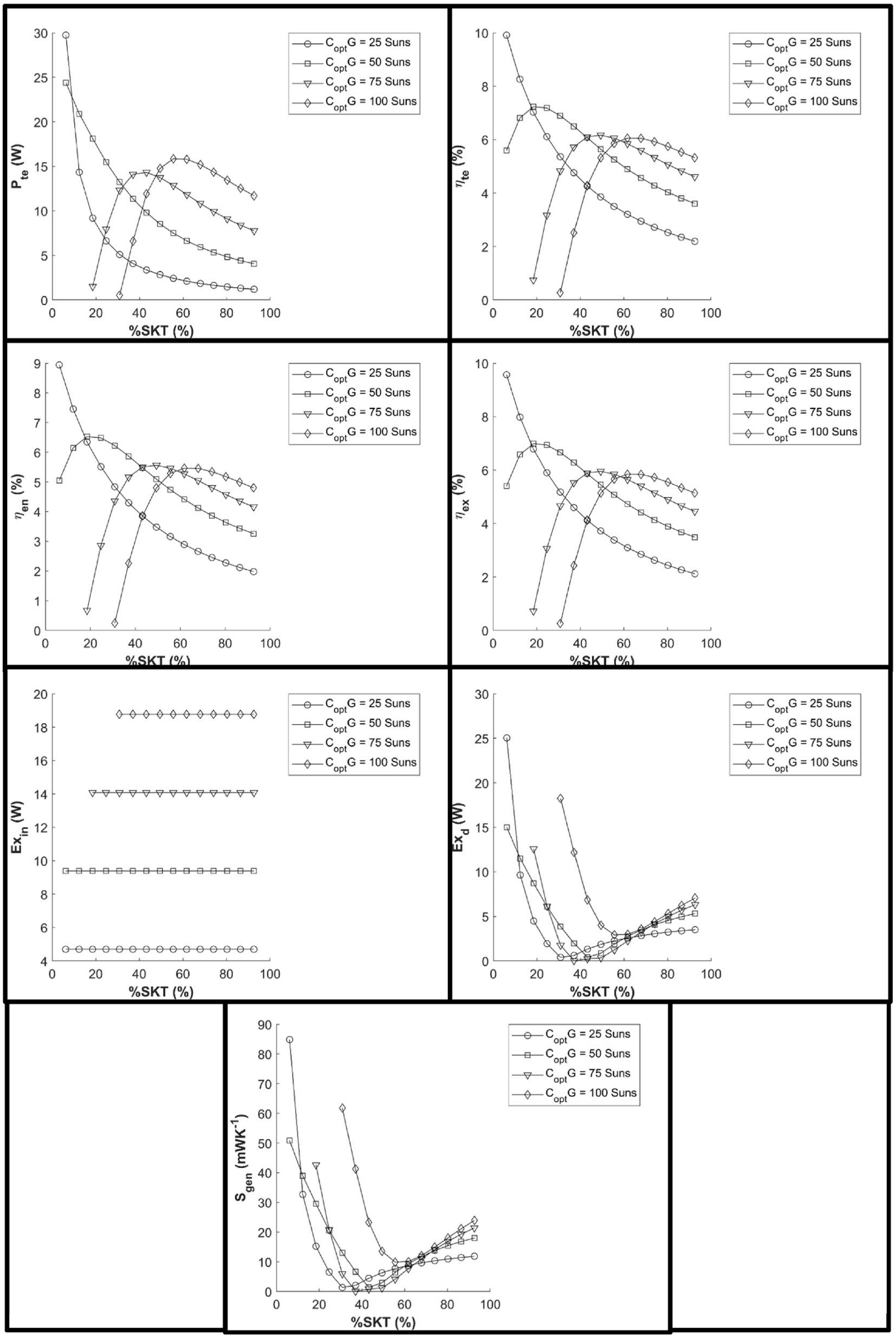

Fig. 14. Consequence of the skutterudite content on the TE power output and conversion efficiency, energy efficiency, exergy efficiency, exergy input, exergy destruction rate, and entropy generation rate.

Table 4
Optimal thermal parameters

Performance	C_{opt}	$h_{conv,c}$ ($kWm^{-2}K^{-1}$)	$h_{conv,h}$ ($Wm^{-2}K^{-1}$)	T_a (K)
P_{te} (W)	93 (14.8)	3 (3.1)	7.8 (2.8)	273 (2.9)
η_{te} (%)	74 (6.2)	3 (4.3)	7.8 (3.8)	273 (4.1)
η_{en} (%)	74 (5.6)	3 (3.9)	7.8 (3.5)	273 (3.7)
η_{ex} (%)	74 (6.0)	3 (4.1)	7.8 (3.7)	273 (3.9)
Ex_d (W)	74 (0.9)	3 (1.6)	7.8 (1.9)	273 (1.8)
S_{gen} (mWK^{-1})	74 (2.9)	3 (5.5)	7.8 (6.5)	273 (6.7)

when the semiconductor cross-section is varied. Meanwhile, maximum efficiencies are reached at a semiconductor cross-section of 0.04 mm^2 and an optimal solar flux of 50 Suns. As observed when the thermoelectric height was increased, the exergy input remains constant, as the heat input stays constant while the cross-section varies.

Lastly, the exergy destruction rate and entropy generation within the thermoelectric system are minimized at an optimal thermoelectric cross-sectional area, which is heavily influenced by the operating concentrated solar flux. The results show that at concentrated solar fluxes of 25 Suns, 50 Suns, 75 Suns, and 100 Suns, the optimum cross-sections are 0.64 mm^2, 1.44 mm^2, 1.69 mm^2, 0.81 mm^2, which minimize the exergy destruction and entropy generation rates to 0.19 W and 0.6 mWK^{-1}, 0.12 W and 0.4 WK^{-1}, 0.2W and 0.66 mWK^{-1}, 0.22 W and 0.7 mWK^{-1}, respectively. These findings indicate that the thermoelectric system's optimal thermodynamic stability is attained at the cross-sectional area and solar flux conditions of 1.44 mm^2 and 50 Suns, respectively. This novel finding improves upon previous knowledge on thermoelectric module entropy and exergy analysis, which assumed that irreversibility increases with operating temperature since they failed to consider the combined impacts of solar flux and cross-section in their analysis. These findings can be explained by considering the sensitivity of the thermoelectric semiconductors to changing temperatures resulting from the applied heat fluxes on the module's hot junction, which were previously neglected in existing literature. Furthermore, it is demonstrated that as the cross-section is varied, the same optimal solar flux (50 Suns) that minimizes the entropy generation also maximizes the efficiencies, albeit at different optimum cross-sections.

3.2.3. Skutterudite content

Previous findings on segmented variable area leg TEGs did not consider the significance of the percentage skutterudite content on the module's performance. Although prior studies on segmented thermoelectric generators have demonstrated the importance of skutterudite content on the overall performance of the device, their findings are not applicable to this study since they focused on a uniform (rectangular) leg geometry. For example Shittu et al. [52] analyzed the effect of non-uniform heat flux on TEG performance, highlighting substantial power output improvements with segmented configurations. The results of this analysis are shown in Fig. 14.

The plot reveals that for low heat fluxes of 25 and 50 Suns, the power output decreases exponentially as the skutterudite percentage increases. However, for higher heat fluxes of 50 and 75 Suns, an optimum skutterudite content exists that yields maximum power from the thermoelectric generator. More specifically, the optimum skutterudite content for maximum power increases as the applied concentrated solar flux intensifies. For low heat fluxes of 25 and 50 Suns, the maximum power outputs achieved were 29.7 W and 24.4 W, respectively, at low skutterudite contents of 6.2 %. For the significantly higher heat fluxes of 75 and 100 Suns, maximum power outputs of 14.3 W and 15.8 W were obtained at optimum skutterudite contents of 43.21 % and 55.56 %, respectively. This indicates a higher requirement for skutterudite to achieve optimum power generation as the concentrated solar flux increases, validating the appropriateness of segmented thermoelectric modules for high-temperature applications.

A similar observation is made for the efficiency plots, where it is demonstrated that the efficiency decreases for low heat fluxes of 25 Suns beyond which an optimum skutterudite content maximizes the efficiency obtained from the system. Using exergy efficiency as a reference, it is noted that at 25 Suns and 6.17 % skutterudite content, the maximum exergy efficiency of 8.9 % is achieved. However, when the heat flux is increased to 50 Suns, 75 Suns, and 100 Suns, the maximum exergy efficiencies of 6.5 %, 5.6 %, and 5.5 % are obtained at optimum skutterudite contents of 18.52 % (SKT), 49.38 % (SKT), and 61.73 % (SKT), respectively. This result further indicates that the maximum exergy efficiency decreases as the thermoelectric module operates under higher solar fluxes, primarily due to the decline the semiconductor thermoelectric material properties under elevated temperatures. Overall, it is noticed that at the lower solar flux of 25 Suns which gives the highest power and efficiency, the optimum skutterudite contents for maximum power and efficiencies exactly coincide at 6.17 %.

While the exergy input remains constant with the skutterudite percentage content, it is observed that the exergy destruction rate and entropy generation are minimized at optimum skutterudite contents, which are heavily influenced by the operating concentrated solar flux. Specifically, for concentrated solar fluxes of 25 Suns, 50 Suns, 75 Suns, and 100 Suns, the minimum exergy destruction and entropy generation rates of 0.4 W and 1.35 mWK^{-1}, 0.42 W and 1.4 mWK^{-1}, 0.02 W and 0.07 mWK^{-1}, 2.92 W and 9.9 mWK^{-1}, were obtained at optimum skutterudite contents of 30.86 %, 43.2 %, 37 %, and 55.56 %, respectively. These results are consistent with the fact that irrespective of the applied solar flux, the optimum skutterudite contents for maximum power/efficiency and minimum exergy destruction/entropy generation are always different. Finally, as expected, the optimum skutterudite content for minimum exergy destruction and entropy generation continually increases as the concentrated solar irradiance rises, indicating the desirability of segmented thermoelectric generators with a higher content of high-temperature materials for optimal performance when exposed to high solar flux applications.

In summary, this study highlights the importance of considering the percentage of skutterudite content when analyzing the performance of segmented variable area leg TEGs, which was not addressed in previous studies. The findings indicate that the optimum

Table 5
Optimal geometry parameters

Parameter	H_{te} (mm)				A_{te} (mm^2)				%SKT (%)			
	25 Suns	50 Suns	75 Suns	100 Suns	25 Suns	50 Suns	75 Suns	100 Suns	25 Suns	50 Suns	75 Suns	100 Suns
P_{te} (W)	5.2 (3.8)	3.2 (9.2)	2.2 (13.3)	1.2 (14.9)	0.04 (10)	0.04 (17.6)	0.16 (21.8)	0.16 (21.4)	6.2 (29.7)	6.2 (24.4)	43.2 (14.3)	55.6 (15.8)
η_{te} (%)	14.2 (9.3)	14.2 (10.3)	14.2 (9.5)	14.2 (7.7)	0.04 (8.3)	0.04 (9.3)	0.04 (8.6)	0.04 (7.2)	6.2 (9.9)	18.5 (7.2)	49.4 (6.2)	62 (6)
η_{en} (%)	14.2 (8.4)	14.2 (9.3)	14.2 (8.5)	14.2 (7)	0.04 (7.5)	0.04 (8.4)	0.04 (7.8)	0.04 (6.5)	6.2 (8.9)	18.5 (6.5)	49.4 (5.6)	62 (5.5)
η_{ex} (%)	14.2 (9.0)	14.2 (10)	14.2 (9.1)	14.2 (7.5)	0.04 (8)	0.04 (9)	0.04 (8.3)	0.04 (6.96)	6.2 (9.6)	18.5 (7)	49.4 (5.9)	62 (5.8)
Ex_d (W)	5.2 (0.88)	3.2 (0.2)	2.2 (0.75)	1.2 (3.8)	0.64 (0.19)	1.44 (0.12)	1.69 (0.2)	0.81 (0.22)	30.9 (0.4)	43.2 (0.42)	37 (0.02)	55.6 (2.92)
S_{gen} (mWK^{-1})	5.2 (3.0)	3.2 (0.7)	2.2 (2.5)	1.2 (13)	0.64 (0.6)	1.44 (0.4)	1.69 (0.66)	0.81 (0.7)	30.9 (1.35)	43.2 (1.4)	37 (0.07)	55.6 (9.9)

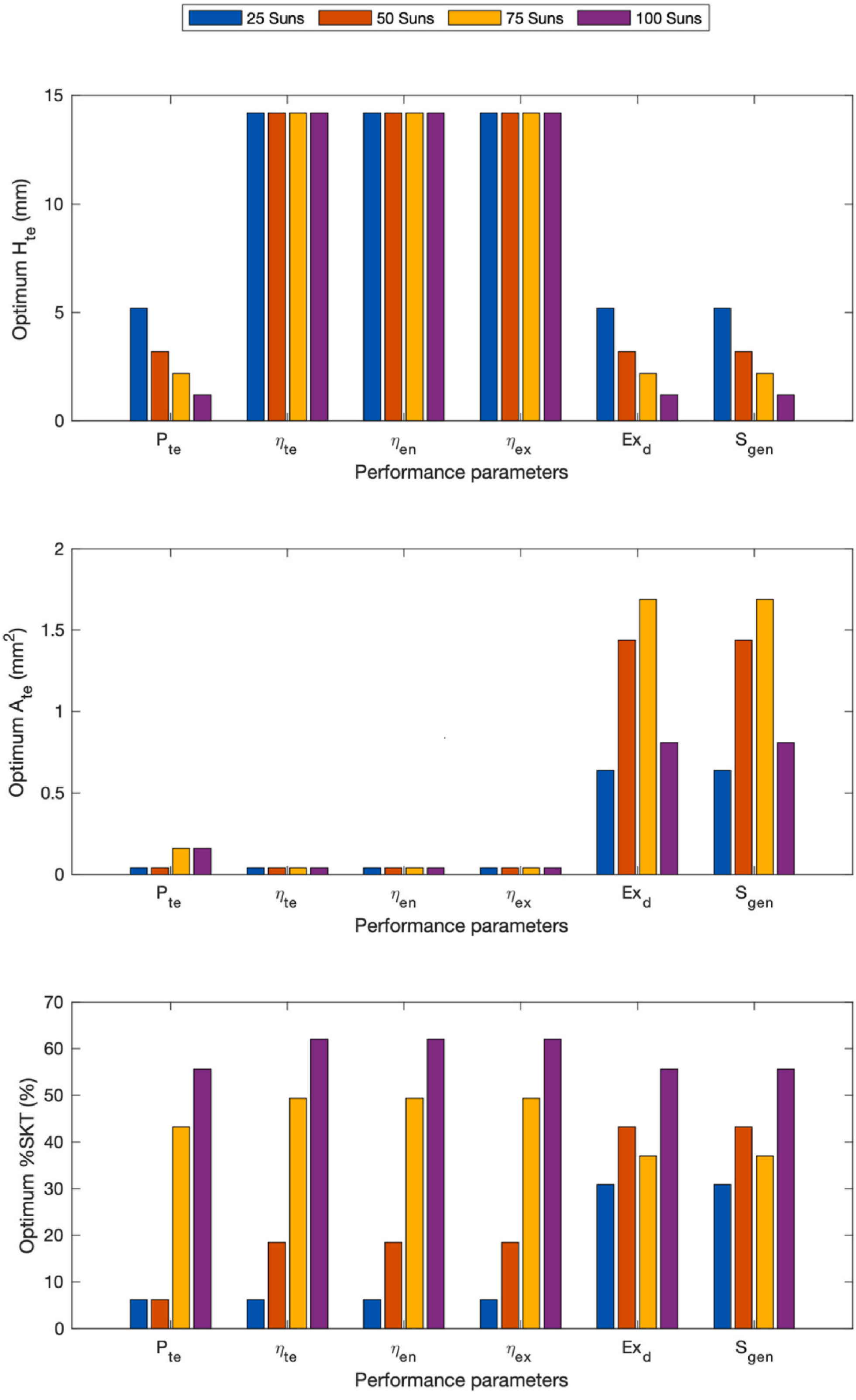

Fig. 15. Optimum geometry parameters for maximum energy and energy efficiency and minimum entropy generation and exergy destruction.

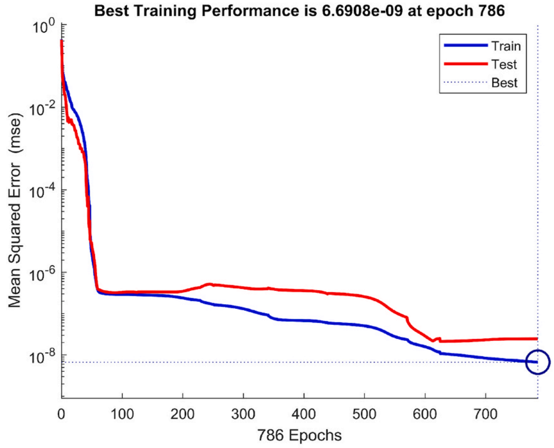

(A)

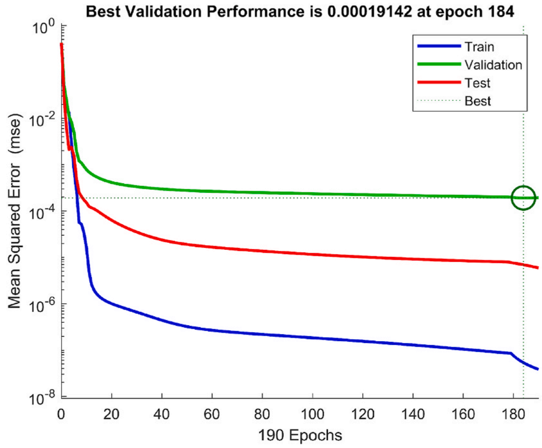

(B)

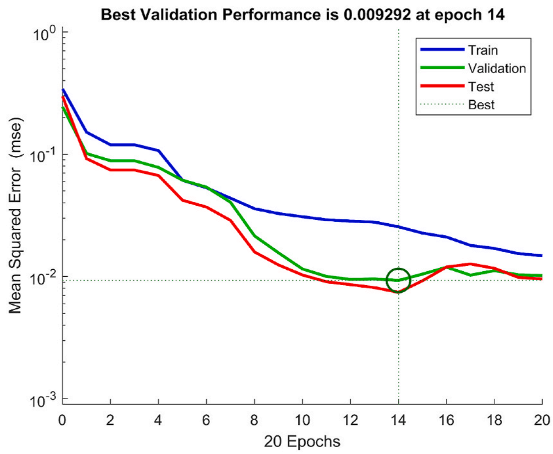

(C)

Fig. 16. Loss function evolution for the neural networks built with the (A) Bayesian regularization (B) Levenberg-Marquardt (C) Scaled Conjugate Gradient.

skutterudite content for maximum power and efficiency is influenced by the operating concentrated solar flux. Moreover, it has been demonstrated that the optimum thermodynamic stability of the thermoelectric system is obtained at a much higher skutterudite content than that required for maximum power and efficiency, emphasizing the necessity of utilizing segmented thermoelectric generators with a higher content of high-temperature materials for optimal performance in high solar flux applications. This insight contributes to a better understanding of the design and optimization of segmented thermoelectric generators, paving the way for more efficient and effective energy conversion devices in solar energy applications.

3.3. Optimal design parameters

In this section, we summarize the optimal design parameters obtained from the numerical optimization scheme. The optimal values for thermal parameters, including the optimal thermal mix and the maximum/minimum performance parameters, are presented in Table 4. The optimal geometry parameters, along with the maximum/minimum performance parameters for the system, are shown in Table 5. Additionally, for a better understanding of the results, a graphical depiction of the optimum geometry parameters is presented in Fig. 15.

3.3.1. Optimal thermal parameters

From the results in Tables 4 and it is evident that the optimal cold and hot junction convective film coefficients and ambient temperature for optimizing the energy, exergy, and entropy performance of the thermoelectric system are the same. However, the optimal optical solar concentration ratios for efficiency and entropy are the same while the one for power is different. This observation suggests that exergy destruction and entropy generation are minimized at the lowest concentration ratio in a thermoelectric system, likely due to thermodynamic irreversibility in the constituent materials at elevated temperatures. However, this results in reduced maximum power, as the optimal solar concentration for maximum power generation of approximately 14.8 W requires a higher solar concentration ratio of 93.

It is also noteworthy that, by employing thermal optimization, the maximum power, energy and exergy efficiencies, and minimum entropy generation were obtained only when the solar concentration ratio was parametrically studied. Specifically, the maximum power of 14.8 W is obtained at a solar concentration ratio of 93, the maximum energy and exergy efficiencies of 5.6 % and 6.0 % are obtained at a solar concentration ratio of 74 Suns, and the minimum exergy destruction and entropy generation rates, at 0.9 W and 2.9 mWK^{-1} are obtained at a solar concentration ratio of 74 Suns. This finding implies that the solar concentration ratio is the most influential thermal parameter for maximizing power and efficiency and minimizing entropy generation and exergy destruction.

3.3.2. Optimal geometry parameters

A visual representation of the optimal geometry parameters of the system is shown in Fig. 15 and the actual values are tabulated in Table 5. From the plot and the table, it is evident that the optimum geometry parameters to maximize the energy and exergy efficiency and minimize the entropy generation vary significantly. Specifically, maximum efficiency requires longer semiconductors of 14.2 mm length, which remain uniform regardless of the applied concentrated solar irradiance. In contrast, the optimum thermoelectric height for maximum power and minimum entropy generation decreases with increasing solar flux, implying that lower optimum heights will be needed as the solar flux intensifies. It is worth noting that the optimum height for maximum power and minimum entropy for all applied heat flux ranges coincide exactly, indicating that maximizing power generation by using the optimum semiconductor height automatically minimizes exergy destruction and entropy generation within the thermoelectric system.

However, when considering the cross-sectional area, it is observed that the optimum area for maximum power and efficiency coincides only for low heat fluxes of 25 and 50 Suns. For 75 and 100 Suns, the optimum area for maximum power becomes slightly larger than that for maximum efficiencies. Nonetheless, the optimum areas for minimum entropy generation are the highest and are strongly influenced by the operating solar flux, with the largest area for 75 Suns and the smallest area for 25 Suns.

Finally, the variation of the optimum skutterudite contents for all performance parameters of the thermoelectric module is presented. It is shown that at 25 Suns, the optimum skutterudite content (6.2 %) for maximum power, thermoelectric efficiency, energy efficiency, and exergy efficiency are all the same. It is also observed that this 6.2 % optimum skutterudite generates the maximum power of 29.7 W and efficiencies of 9.9 %, 8.9 %, and 9.6 % for the thermoelectric, energy, and exergy efficiencies, respectively. Nevertheless, the minimum entropy generation and exergy destruction of 0.02 W and 0.07 mWK^{-1}, respectively, are obtained at a higher heat flux of 75 Suns when a 37 % skutterudite content is used. This suggests that a higher solar flux and skutterudite content, more than that required for power and efficiency, are necessary to minimize the thermodynamic irreversibility of the system. Finally, these results indicates that of all parameters considered in this study, the percentage skutterudite content has the most significant influence on the energy, exergy, and entropy performance of the system.

3.4. Neural network performance

This section presents the properties of ANN models developed using three training algorithms to accurately predict the performance of the thermoelectric module. The performance of the three ANNs is then evaluated using mean squared error and the coefficient of determination as metrics. Lastly, the impact of varying the number of neurons in the Bayesian regularized ANN selected as the optimum ANN model is explored.

3.4.1. Loss function evolution

The loss function (mean squared error) evolution of the neural networks constructed with the three training algorithms is illustrated in Fig. 16. The results generally show that the LM and SCG ANNs have training, testing, validation, and all datasets, while the BR ANN does not have a validation dataset. This is consistent with literature findings, which reported that the BR ANN eliminates the need

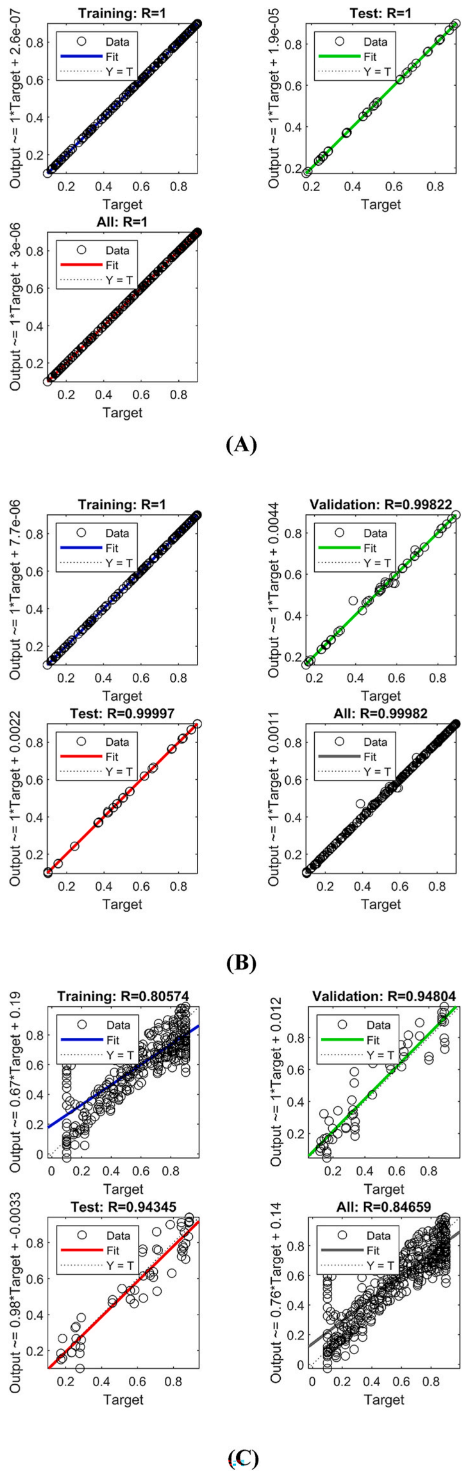

Fig. 17. Coefficient of determination for the neural networks built with the (A) Bayesian regularization (B) Levenberg-Marquardt (C) Scaled Conjugate Gradient.

for a lengthy cross-validation dataset [53], prevents overfitting of the data by introducing uncertainty in the model's prediction, builds an accurate model with fewer data points, offers better generalization, and is more resilient to noisy datasets. It is important to note that the advantages of BR ANNs come at the expense of increased computational complexity during training, as the Bayesian framework involves updating and maintaining probability distributions for each weight in the network. However, in many cases, the benefits of using a BR ANN outweigh the additional computational cost. This is evident in the plot since the BR ANN yields the lowest

Table 6
Network training information of the neural network

Neurons	Epochs	Elapsed time	Performance	Gradient	Mu	Effective number of parameters	Sum squared parameters
10	786	12 s	6.69×10^{-9}	9.95×10^{-8}	50	308	167
30	345	53 s	1.82×10^{-9}	1.00×10^{-7}	50	319	155
60	691	18 min, 39 s	2.13×10^{-9}	9.98×10^{-8}	50	323	159
90	1000	1 h, 43 min, 39 s	2.99×10^{-10}	1.82×10^{-7}	50	351	155

mean squared error of 6.7×10^{-9} after 786 epochs. Conversely, the LM and SCG ANNs had higher mean squared errors of 1.9×10^{-4} after 184 epochs and 9.3×10^{-3} after 14 epochs, respectively. This demonstrates that the BR ANN is 100 % more accurate than the widely used LM ANN for predicting the performance of thermoelectric modules.

3.4.2. *Coefficient of determination*

To further demonstrate the accuracy of the BR ANN, the coefficients of determination (CODs) of the three ANNs are presented in Fig. 17. Due to the effective generalization of the BR ANN, it is observed that the COD for the training and testing datasets are 100 %, indicating a perfect fit with the numerical data in all cases. For the LM ANN, the COD for the training dataset was 100 %; however, some outliers in the validation dataset ultimately appear in the numerical (all) dataset, resulting in a 99.98 % COD. Lastly, the SCG ANN has the lowest COD values of 80.57 %, 94.8 %, 94.34 %, and 84.66 % for the training, validation, test, and numerical (all) datasets, respectively, which can be attributed to the high mean squared error reported earlier.

3.5. *Effect of neurons*

This section examines the effects of varying the number of neurons (10, 30, 60, and 90) on the performance of the BR ANN, while other hyperparameters are kept constant. The results of this analysis are provided in Table 6. The first observation is that the training time increases with the number of neurons due to the higher complexity of the network. Additionally, the ANN's performance improves as the mean squared error decreases with an increasing number of neurons, which can be attributed to the increased complexity of the model, making it more sensitive to patterns in the data. However, this comes at the expense of increased computational time.

The rise in network complexity is evident with the increase in the number of neurons, while the sum squared parameters decrease as the number of neurons increase. Note that the effective number of parameters represents the significant parameters used for estimating the model's complexity, while the sum squared parameters stand for the weights and biases used as a regularization term to prevent overfitting by penalizing large parameter values. Moreover, the constant mu parameter at 50, regardless of the number of neurons, suggests that the prior mean of the weights and biases is the same across different network configurations. In our study, we opt for the model with 10 neurons since it has the shortest elapsed time (12 s) and very low performance on the numerical data (6.7×10^{-9}) while also having the smallest effective number of parameters (308), and highest number of sums squared parameters (167) indicating low complexity with high accuracy.

3.6. *Replication of experiments*

To authenticate the numerical representation of the innovative full-scale segmented variable area leg thermoelectric module, experimental and numerical findings from pertinent studies were juxtaposed with the current numerical model. The experimental investigation by Fabián-Mijangos et al. [24], which confirmed the enhanced performance of variable area leg thermoelectric generators (Trap) relative to uniform leg thermoelectric generators (Rect), was employed for validation purpose.

Fig. 18 presents the outcomes of the comparative analysis, illustrating a close correlation between the numerical and experimental findings, with a maximum relative error of 2.4 % observed in Fig. 18A and D. This signifies a satisfactory performance of the numerical model, accompanied by a low relative error. The juxtaposition with prior relevant experimental and numerical results substantiates the accuracy of the current numerical model and highlights its capacity for optimizing the performance of the full-scale thermoelectric module examined in this research.

4. Conclusions

In conclusion, this research contributes substantially to renewable energy technology by advancing the design and optimization of segmented variable area leg TEGs for concentrated solar power applications.

- **Innovative Analytical Approach**: A unique integration of numerical analysis and ANNs was employed to scrutinize geometric and thermal parameters, including semiconductor height, cross-sectional area, skutterudite content, solar concentration ratio, and convective heat transfer coefficients. This methodology empowers high-fidelity performance analysis and optimization in a renewable energy context.
- **Material Optimization**: The study establishes skutterudite content as a pivotal material parameter. Specifically, a 6.2 % content under 25 Suns yields the highest power output (29.7 W) and efficiencies of 9.9 % (thermoelectric), 8.9 % (energy), and 9.6 % (exergy). Conversely, minimized entropy generation and exergy destruction were observed at 75 Suns with a 37 % content.
- **Solar Concentration Significance**: The research accentuates the solar concentration ratio as an indispensable thermal parameter. A ratio of 74 Suns emerged as the optimum, maximizing efficiency and minimizing entropy generation and exergy destruction.

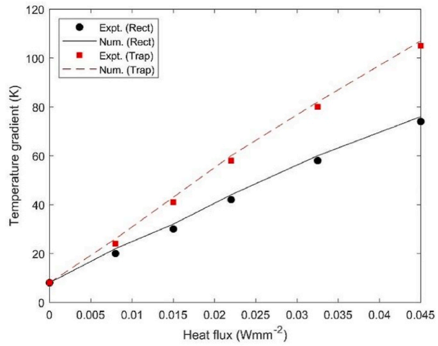

(A)

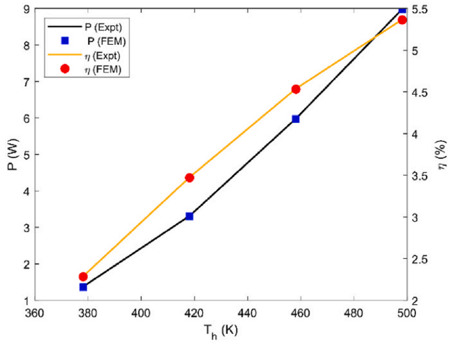

(B)

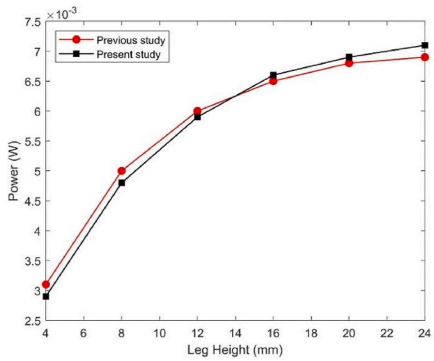

(C)

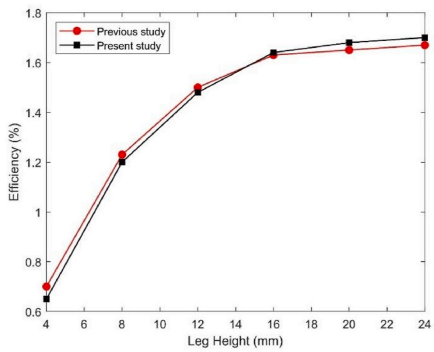

(D)

Fig. 18. Replication of experimental results (A) Fabián-Mijangos et al. [24] (B) [54] (C, D [54].

- **Computational Efficiency via ANNs**: Amongst ANNs with different training algorithms, the BR ANN exhibited exemplary accuracy and computational efficiency, achieving a coefficient of determination of 100 % with a mean squared error of 6.7×10^{-9}.
- **Implications for Renewable Energy**: The insights gleaned through this research serve as a catalyst for the development of cutting-edge segmented TEGs, bolstering their performance in solar energy harnessing. By incorporating optimized skutterudite content and solar concentration ratios, along with geometric refinements, a new frontier for efficient renewable energy conversion can be realized.

These findings are integral to the ongoing efforts in the renewable energy sector to optimize and enhance the efficacy of solar thermoelectric generators.

5. Future research directions

Building upon the insights gained from this study, there are several promising avenues for future research to further advance the development and optimization of segmented TEGs for solar energy applications.

- *Material advancements*: Investigate the potential of newly developed or improved thermoelectric materials that may offer higher conversion efficiencies or better stability under high temperature and concentrated solar flux conditions.
- *Hybrid systems*: Explore the integration of TEGs with other renewable energy technologies, such as photovoltaic (PV) cells or solar thermal systems, to create hybrid energy conversion systems that capitalize on the strengths of each technology while minimizing their limitations.
- *Advanced optimization techniques*: Apply more sophisticated optimization algorithms, such as genetic algorithms, particle swarm optimization, or simulated annealing, to further optimize the geometry, material composition, and operating conditions of segmented TEGs.
- *Dynamic operation*: Investigate the performance of segmented TEGs under varying solar irradiance and ambient temperature conditions, simulating real-world operation and accounting for diurnal and seasonal variations in solar energy availability.
- *System-level analysis*: Conduct a comprehensive analysis of the entire concentrated solar power system, including the solar concentrator, heat transfer fluids, and thermal storage, to optimize the overall system performance and identify potential synergies between components.
- *Economic and environmental assessments*: Carry out cost-benefit analyses and life cycle assessments to evaluate the economic viability and environmental impact of using segmented TEGs in solar energy applications, considering factors such as material availability, manufacturing costs, and waste disposal.
- *Scalability and manufacturability*: Investigate the scalability of the optimized segmented TEG designs for large-scale deployment in solar power plants, as well as the feasibility of mass production and the potential challenges associated with manufacturing and assembly processes.

By addressing these research areas, the development and application of segmented TEGs in solar energy systems can be further advanced, ultimately leading to more efficient and sustainable energy conversion technologies that contribute to global efforts in combating climate change and securing a clean energy future.

CRediT authorship contribution statement

Hisham Alghamdi: Supervision, Funding acquisition, Conceptualization. **Chika Maduabuchi:** Writing – review & editing, Writing – original draft, Conceptualization. **Kingsley Okoli:** Data curation, Formal analysis, Writing – review & editing. **Abdullah Albaker:** Methodology, Software. **Mohammad Alobaid:** Validation, Investigation. **Mohammed Alghassab:** Resources, Project administration. **Emad Makki:** Visualization, Supervision. **Mohammad Alkhedher:** Data curation, Investigation.

Declaration of competing interest

The authors declare that they have no known competing financial interests or personal relationships that could have appeared to influence the work reported in this paper.

Data availability

Data will be made available on request.

Acknowledgements

The Deanship of Scientific Research at Najran University for funding this work under the grant code (NU/NRP/SERC/12/16), the Deanship of Scientific Research at Shaqra University for supporting this work, the Deanship of Scientific Research, Majmaah University, Saudi Arabia for funding this research work through the project number (000-2023-000), the Office of Research and Sponsored Programs (ORSP) at Abu Dhabi University for funding this paper through a research fund.

Appendix A. Supplementary data

Supplementary data to this article can be found online at https://doi.org/10.1016/j.csite.2024.104940.

References

[1] M.R. Burton, S. Mehraban, D. Beynon, J. McGettrick, T. Watson, N.P. Lavery, M.J. Carnie, 3D printed SnSe thermoelectric generators with high figure of merit, Adv. Energy Mater. 9 (2019), https://doi.org/10.1002/aenm.201900201.
[2] W. Li, J. Wang, Y. Xie, J.L. Gray, J.J. Heremans, H.B. Kang, B. Poudel, S.T. Huxtable, S. Priya, Enhanced thermoelectric performance of Yb-Single-Filled skutterudite by ultralow thermal conductivity. https://doi.org/10.1021/acs.chemmater.8b03994, 2019.
[3] R. Yanagisawa, N. Tsujii, T. Mori, P. Ruther, O. Paul, M. Nomura, Nanostructured planar-type uni-leg Si thermoelectric generators, APEX 13 (2020) 095001, https://doi.org/10.35848/1882-0786/aba5c4.
[4] H.J. Goldsmid, Improving the thermoelectric figure of merit, Sci. Technol. Adv. Mater. 22 (2021) 280–284, https://doi.org/10.1080/14686996.2021.1903816.
[5] T. Zhu, Y. Liu, C. Fu, J.P. Heremans, J.G. Snyder, X. Zhao, Compromise and synergy in high-efficiency thermoelectric materials, Adv. Mater. 29 (2017) 1605884, https://doi.org/10.1002/adma.201605884.
[6] H.J. Goldsmid, R.W. Douglas, The use of semiconductors in thermoelectric refrigeration, Br. J. Appl. Phys. 5 (1954) 386, https://doi.org/10.1088/0508-3443/5/11/303.
[7] C. Uher (Ed.), Materials Aspect of Thermoelectricity, CRC Press, Boca Raton, 2016, https://doi.org/10.1201/9781315197029.
[8] F. Li, R. Zhai, Y. Wu, Z. Xu, X. Zhao, T. Zhu, Enhanced thermoelectric performance of n-type bismuth-telluride-based alloys via in alloying and hot deformation for mid-temperature power generation, Journal of Materiomics 4 (2018) 208–214, https://doi.org/10.1016/j.jmat.2018.05.008.
[9] B. Poudel, Q. Hao, Y. Ma, Y. Lan, A. Minnich, B. Yu, X. Yan, D. Wang, A. Muto, D. Vashaee, X. Chen, J. Liu, M.S. Dresselhaus, G. Chen, Z. Ren, High-thermoelectric performance of nanostructured bismuth antimony telluride bulk alloys, Science 320 (2008) 634–638, https://doi.org/10.1126/science.1156446.
[10] X. Shi, Jiong Yang, J.R. Salvador, M. Chi, J.Y. Cho, H. Wang, S. Bai, Jihui Yang, W. Zhang, L. Chen, Multiple-filled skutterudites: high thermoelectric figure of merit through separately optimizing electrical and thermal transports, J. Am. Chem. Soc. 134 (2012) 2842, https://doi.org/10.1021/ja211185w, 2842.
[11] K. Biswas, J. He, I.D. Blum, C.-I. Wu, T.P. Hogan, D.N. Seidman, V.P. Dravid, M.G. Kanatzidis, High-performance bulk thermoelectrics with all-scale hierarchical architectures, Nature 489 (2012) 414–418, https://doi.org/10.1038/nature11439.
[12] C. Fu, S. Bai, Y. Liu, Y. Tang, L. Chen, X. Zhao, T. Zhu, Realizing high figure of merit in heavy-band p-type half-Heusler thermoelectric materials, Nat. Commun. 6 (2015) 8144, https://doi.org/10.1038/ncomms9144.
[13] D. Luo, Y. Yan, W.-H. Chen, X. Yang, H. Chen, B. Cao, Y. Zhao, A comprehensive hybrid transient CFD-thermal resistance model for automobile thermoelectric generators, Int. J. Heat Mass Tran. 211 (2023) 124203, https://doi.org/10.1016/j.ijheatmasstransfer.2023.124203.
[14] L.I. Anatychuk, L.N. Vikhor, Physics and methods of FGTM design, in: Proceedings ICT'03. 22nd International Conference on Thermoelectrics (IEEE Cat. No.03TH8726). Presented at the Proceedings ICT'03. 22nd International Conference on Thermoelectrics, IEEE Cat. No.03TH8726), 2003, pp. 425–428, https://doi.org/10.1109/ICT.2003.1287539.
[15] V.L. Kuznetsov, L.A. Kuznetsova, A.E. Kaliazin, D.M. Rowe, High performance functionally graded and segmented Bi2Te3-based materials for thermoelectric power generation, J. Mater. Sci. 37 (2002) 2893–2897, https://doi.org/10.1023/A:1016092224833.
[16] L. Fan, G. Zhang, R. Wang, K. Jiao, A comprehensive and time-efficient model for determination of thermoelectric generator length and cross-section area, Energy Convers. Manag. 122 (2016) 85–94, https://doi.org/10.1016/j.enconman.2016.05.064.
[17] Y. Luo, C.N. Kim, Effects of the cross-sectional area ratios and contact resistance on the performance of a cascaded thermoelectric generator, Int. J. Energy Res. 43 (2019) 2172–2187, https://doi.org/10.1002/er.4426.
[18] A. Yusuf, N. Bayhan, A.A. Ibrahim, H. Tiryaki, S. Ballikaya, Geometric optimization of thermoelectric generator using genetic algorithm considering contact resistance and Thomson effect, Int. J. Energy Res. 45 (2021) 9382–9395, https://doi.org/10.1002/er.6467.
[19] S. Ferreira-Teixeira, A.M. Pereira, Geometrical optimization of a thermoelectric device : numerical simulations, Energy Convers. Manag. 169 (2018) 217–227, https://doi.org/10.1016/j.enconman.2018.05.030.
[20] A.F. Ioffe, Semiconductor Thermoelements and Thermoelectric Cooling, Infosearch Ltd, 1957.
[21] J.A. Brandt, Solutions to the differential equations describing the temperature distribution, thermal efficiency, and power output of a thermoelectric element with variable properties and cross sectional area, Adv. Energy Convers. 2 (1962) 219–230, https://doi.org/10.1016/0365-1789(62)90026-7.
[22] H. Ali, B.S. Yilbas, A.Z. Sahin, Exergy analysis of a thermoelectric power generator: influence of bi-tapered pin geometry on device characteristics, Int. J. Exergy 16 (2015) 53–71, https://doi.org/10.1504/IJEX.2015.067299.
[23] O.I. Ibeagwu, Modelling and comprehensive analysis of TEGs with diverse variable leg geometry, Energy 180 (2019) 90–106, https://doi.org/10.1016/j.energy.2019.05.088.
[24] A. Fabián-Mijangos, G. Min, J. Alvarez-Quintana, Enhanced performance thermoelectric module having asymmetrical legs, Energy Convers. Manag. 148 (2017) 1372–1381, https://doi.org/10.1016/j.enconman.2017.06.087.
[25] W.-H. Chen, Y.-B. Chiou, Geometry design for maximizing output power of segmented skutterudite thermoelectric generator by evolutionary computation, Appl. Energy 274 (2020) 115296, https://doi.org/10.1016/j.apenergy.2020.115296.
[26] H.B. Liu, J.H. Meng, X.D. Wang, W.H. Chen, A new design of solar thermoelectric generator with combination of segmented materials and asymmetrical legs, Energy Convers. Manag. 175 (2018) 11–20, https://doi.org/10.1016/j.enconman.2018.08.095.
[27] S. Shittu, G. Li, X. Zhao, X. Ma, Y. Golizadeh, E. Ayodele, Optimized high performance thermoelectric generator with combined segmented and asymmetrical legs under pulsed heat input power, J. Power Sources 428 (2019) 53–66, https://doi.org/10.1016/j.jpowsour.2019.04.099.
[28] Y.-Q. Zhang, J. Sun, G.-X. Wang, T.-H. Wang, Advantage of a thermoelectric generator with hybridization of segmented materials and irregularly variable cross-section design, Energies 15 (2022) 2944, https://doi.org/10.3390/en15082944.
[29] O. Bamisile, A. Oluwasanmi, S. Obiora, E. Osei-Mensah, G. Asoronye, Q. Huang, Application of deep learning for solar irradiance and solar photovoltaic multi-parameter forecast, Energy Sources, Part A Recovery, Util. Environ. Eff. (2020) 1–21, https://doi.org/10.1080/15567036.2020.1801903.
[30] M. Zhang, Y. Tian, H. Xie, Z. Wu, Y. Wang, Influence of Thomson effect on the thermoelectric generator, Int. J. Heat Mass Tran. 137 (2019) 1183–1190, https://doi.org/10.1016/j.ijheatmasstransfer.2019.03.155.
[31] Y. Luo, L. Li, Y. Chen, C.N. Kim, Influence of geometric parameter and contact resistances on the thermal-electric behavior of a segmented TEG, Energy 254 (2022) 124487, https://doi.org/10.1016/j.energy.2022.124487.
[32] S. Sripadmanabhan Indira, C.A. Vaithilingam, R. Sivasubramanian, K.-K. Chong, R. Saidur, K. Narasingamurthi, Optical performance of a hybrid compound parabolic concentrator and parabolic trough concentrator system for dual concentration, Sustain. Energy Technol. Assessments 47 (2021) 101538, https://doi.org/10.1016/j.seta.2021.101538.
[33] K.A. Mazzio, C.K. Luscombe, The future of organic photovoltaics, Chem. Soc. Rev. 44 (2014) 78–90, https://doi.org/10.1039/C4CS00227J.
[34] T. Yang, J. Xiao, P. Li, P. Zhai, Q. Zhang, Simulation and optimization for system integration of a solar thermoelectric device, J. Electron. Mater. 40 (2011) 967–973, https://doi.org/10.1007/s11664-010-1471-2.
[35] C. Maduabuchi, Improving the performance of a solar thermoelectric generator using nano-enhanced variable area pins, Appl. Therm. Eng. 206 (2022) 118086, https://doi.org/10.1016/j.applthermaleng.2022.118086.
[36] G. Notton, C. Cristofari, M. Mattei, P. Poggi, Modelling of a double-glass photovoltaic module using finite differences, Appl. Therm. Eng. 25 (2005) 2854–2877, https://doi.org/10.1016/j.applthermaleng.2005.02.008.

[37] C. Maduabuchi, C. Eneh, A.A. Alrobaian, M. Alkhedher, Deep neural networks for quick and precise geometry optimization of segmented thermoelectric generators, Energy 263 (2023) 125889, https://doi.org/10.1016/j.energy.2022.125889.
[38] H. Alghamdi, C. Maduabuchi, A. Albaker, I. Alatawi, T.R. Alsenani, A.S. Alsafran, A. Almalaq, M. AlAqil, M.A.H. Abdelmohimen, M. Alkhedher, Corrigendum to "A prediction model for the performance of solar photovoltaic-thermoelectric systems utilizing various semiconductors via optimal surrogate machine learning methods", Engineering Science and Technology, an International Journal 47 (2023) 101546 https://doi.org/10.1016/j.jestch.2023.101546 [Eng. Sci. Technol., Int. J., 40 (2023) 101363].
[39] M.N. Eke, C.C. Maduabuchi, R. Lamba, H.O. Njoku, X. Ma, Y.G. Gurevich, S.K. Tyagi, O.V. Ekechukwu, E.C. Ejiogu, C.T. Eneh, Exergy analysis and optimisation of a two-stage solar thermoelectric generator with tapered legs, Int. J. Exergy 38 (2022) 110, https://doi.org/10.1504/IJEX.2022.122309.
[40] A. Ab-Belkhair, J. Rahebi, A. Abdulhamed Mohamed Nureddin, A study of deep neural network controller-based power quality improvement of hybrid PV/Wind systems by using smart inverter, Int. J. Photoenergy (2020), https://doi.org/10.1155/2020/8891469, 2020.
[41] M. Saeed, A Gentle Introduction to Sigmoid Function, 2021. MachineLearningMastery.com. URL, https://machinelearningmastery.com/a-gentle-introduction-to-sigmoid-function/, 4.23.23.
[42] D.W. Marquardt, An algorithm for least-squares estimation of nonlinear parameters, J. Soc. Ind. Appl. Math. 11 (1963) 431–441, https://doi.org/10.1137/0111030.
[43] M.R. Hestenes, E. Stiefel, Methods of conjugate gradients for solving linear systems, Journal of Research of the National Bureau of Standards 49 (2013) 409–436, https://doi.org/10.6028/jres.049.044.
[44] P. Concus, G. Golub, G. Meurant, Block preconditioning for the conjugate gradient method, SIAM J. Sci. Stat. Comput. 6 (1985) 220–252, https://doi.org/10.1137/0906018.
[45] D.J.C. MacKay, A practical bayesian framework for backpropagation networks, Neural Comput. 4 (1992) 448–472, https://doi.org/10.1162/neco.1992.4.3.448.
[46] D.J.C. MacKay, Bayesian interpolation, Neural Comput. 4 (1992) 415–447, https://doi.org/10.1162/neco.1992.4.3.415.
[47] J. Shi, Y. Zhu, F. Khan, G. Chen, Application of Bayesian Regularization Artificial Neural Network in explosion risk analysis of fixed offshore platform, J. Loss Prev. Process. Ind. 57 (2019) 131–141, https://doi.org/10.1016/j.jlp.2018.10.009.
[48] J.E. Dennis, R.B. Schnabel, 6. Globally Convergent Modifications of Newton's Method, in: Numerical Methods for Unconstrained Optimization and Nonlinear Equations, Classics in Applied Mathematics, Society for Industrial and Applied Mathematics, 1996, pp. 111–154, https://doi.org/10.1137/1.9781611971200.ch6.
[49] I.N. Da Silva, D. Hernane Spatti, R. Andrade Flauzino, L.H.B. Liboni, S.F. Dos Reis Alves, Artificial Neural Networks, Springer International Publishing, Cham, 2017, https://doi.org/10.1007/978-3-319-43162-8.
[50] M. Alobaid, C. Maduabuchi, A. Albaker, A. Almalaq, M. Alanazi, T. Alsuwian, Machine learning and numerical simulations for electrical, thermodynamic, and mechanical assessment of modified solar thermoelectric generators, Appl. Therm. Eng. 220 (2023) 119706, https://doi.org/10.1016/j.applthermaleng.2022.119706.
[51] R. Petela, Exergy of undiluted thermal radiation, Sol. Energy 74 (2003) 469–488, https://doi.org/10.1016/S0038-092X(03)00226-3.
[52] S. Shittu, G. Li, Q. Xuan, X. Zhao, X. Ma, Y. Cui, Electrical and mechanical analysis of a segmented solar thermoelectric generator under non-uniform heat flux, Energy 199 (2020) 117433, https://doi.org/10.1016/j.energy.2020.117433.
[53] Z. Sun, Y. Chen, X. Li, X. Qin, H. Wang, A Bayesian regularized artificial neural network for adaptive optics forecasting, Opt Commun. 382 (2017) 519–527, https://doi.org/10.1016/j.optcom.2016.08.035.
[54] X. Wang, J. Qi, W. Deng, G. Li, X. Gao, L. He, S. Zhang, An optimized design approach concerning thermoelectric generators with frustum-shaped legs based on three-dimensional multiphysics model, Energy 233 (2021) 120810, https://doi.org/10.1016/j.energy.2021.120810.